SISSA

Performance of missing transverse momentum reconstruction in proton-proton collisions at $\sqrt{s}$ = 13 TeV using the CMS detector

View the article online for updates and enhancements.

Recent citations

- Search for long-lived particles using delayed photons in proton-proton collisions at s=13 TeV
  A. M. Sirunyan *et al*

- Search for anomalous electroweak production of vector boson pairs in association with two jets in proton-proton collisions at 13 TeV
  A.M. Sirunyan *et al*

- Supersymmetry and the collider dark matter picture
  Jeanette Miriam Lorenz

Performance of missing transverse momentum reconstruction in proton-proton collisions at $\sqrt{s} = 13\,\text{TeV}$ using the CMS detector

The CMS collaboration

E-mail: cms-publication-committee-chair@cern.ch

ABSTRACT: The performance of missing transverse momentum ($\vec{p}_\mathrm{T}^{\,\text{miss}}$) reconstruction algorithms for the CMS experiment is presented, using proton-proton collisions at a center-of-mass energy of 13 TeV, collected at the CERN LHC in 2016. The data sample corresponds to an integrated luminosity of $35.9\,\text{fb}^{-1}$. The results include measurements of the scale and resolution of $\vec{p}_\mathrm{T}^{\,\text{miss}}$, and detailed studies of events identified with anomalous $\vec{p}_\mathrm{T}^{\,\text{miss}}$. The performance is presented of a $\vec{p}_\mathrm{T}^{\,\text{miss}}$ reconstruction algorithm that mitigates the effects of multiple proton-proton interactions, using the "pileup per particle identification" method. The performance is shown of an algorithm used to estimate the compatibility of the reconstructed $\vec{p}_\mathrm{T}^{\,\text{miss}}$ with the hypothesis that it originates from resolution effects.

Contents

1 Introduction

Weakly interacting neutral particles produced in proton-proton (pp) collisions at the LHC traverse the collider detectors unobserved. However, when such particles are produced along with strong or electromagnetically interacting particles, their presence can be inferred through the measured momentum imbalance in the plane perpendicular to the beam direction, which is referred to as the missing transverse momentum ($\vec{p}_\mathrm{T}^{\mathrm{miss}}$), and its magnitude is $p_\mathrm{T}^{\mathrm{miss}}$.

The precise determination of $p_\mathrm{T}^{\mathrm{miss}}$ is critical for standard model (SM) measurements that use final states with neutrinos, such as those containing leptonic decays of the W boson. In addition, $p_\mathrm{T}^{\mathrm{miss}}$ is one of the most important observables in searches for physics beyond the SM that target new weakly interacting particles. The $\vec{p}_\mathrm{T}^{\mathrm{miss}}$ stemming from weakly interacting particles will be collectively referred to as "genuine $p_\mathrm{T}^{\mathrm{miss}}$" in what follows. However, $p_\mathrm{T}^{\mathrm{miss}}$ reconstruction is sensitive to the experimental resolutions, to mismeasurements of reconstructed particles, and to detector artifacts. The performance of $p_\mathrm{T}^{\mathrm{miss}}$ is also affected by additional pp interactions in the same or nearby bunch crossings (pileup). A detailed understanding of all these effects, both in real and simulated data, is important to achieve optimal $p_\mathrm{T}^{\mathrm{miss}}$ performance.

In this paper, we present studies of $p_\mathrm{T}^{\mathrm{miss}}$ reconstruction algorithms using Monte Carlo simulation, and data collected in 2016 with the CMS detector [1] at the LHC [2], corresponding to an integrated luminosity of 35.9 fb^{-1}, and are applicable to the 2015–2018 data-taking period (LHC Run 2). A brief overview of the CMS detector is given in section 2. Information about event reconstruction is discussed in section 3, and a description of the different $p_\mathrm{T}^{\mathrm{miss}}$ reconstruction algorithms is provided in section 4. Information about event simulation and selection is provided in sections 5 and 6. In section 7, sources of anomalous $p_\mathrm{T}^{\mathrm{miss}}$ measurements from detector and reconstruction artifacts, and methods for identifying and mitigating them, are described. The performance of the $p_\mathrm{T}^{\mathrm{miss}}$ reconstruction at the trigger level is discussed in section 8. Section 9 details the performance of the $p_\mathrm{T}^{\mathrm{miss}}$ algorithms in events with and without genuine $p_\mathrm{T}^{\mathrm{miss}}$. The algorithm that provides an estimate of the $p_\mathrm{T}^{\mathrm{miss}}$ significance is described in section 10. A summary is given in section 11.

2 The CMS detector

The central feature of the CMS apparatus is a superconducting solenoid of 6 m internal diameter, providing a magnetic field of 3.8 T. Within the solenoid volume are a silicon pixel and strip tracker, a lead tungstate crystal electromagnetic calorimeter (ECAL), and a brass and scintillator hadron calorimeter (HCAL), each composed of a barrel and two endcap sections. The pseudorapidity (η) coverage of the ECAL (HCAL) barrel is $|\eta| < 1.479$ ($|\eta| < 1.3$) and endcap is $1.479 < |\eta| < 3.0$ ($1.3 < |\eta| < 3.0$) respectively. Forward hadronic calorimeter (HF) extend the η coverage up to $|\eta| < 5.2$.

In the ECAL and HCAL barrel region, the HCAL cells have widths of 0.087 in η and 0.087 radians in azimuth (ϕ). In the η-ϕ plane, and for $|\eta| < 1.479$, the HCAL cells map on to 5×5 ECAL crystal arrays (supercrystals) to form calorimeter towers projecting radially outwards from close to the nominal interaction point. In the ECAL and HCAL endcap regions, the coverage of the towers increases progressively to a maximum of 0.174 in $\Delta\eta$ and $\Delta\phi$. Within each tower, the energy deposits in ECAL and HCAL cells are summed to define the calorimeter tower energies [1], subsequently used to provide the energies and directions of hadronic jets.

The silicon tracker measures charged particles within the range $|\eta| < 2.5$ (tracker acceptance). It consists of 1440 silicon pixel and 15 148 silicon strip detector modules. Tracks with transverse momentum p_T of $\approx 100\,\text{GeV}$ emitted within $|\eta| < 1.4$ have p_T and impact parameter resolutions of 2.8% and 10 (20) μm in the transverse (longitudinal) direction [3].

Muons are measured in the range $|\eta| < 2.4$, with detection planes made using three technologies: drift tubes in the barrel, cathode strip chambers (CSC) in the endcaps, and resistive plate chambers both in the barrel and in the endcaps embedded in the iron flux-return yoke outside the solenoid [4].

Events of interest are selected using a two-tiered trigger system [5]. The first level (L1), composed of custom hardware processors, uses information from the calorimeters and muon detectors to select events at a rate of around 100 kHz. The second level, known as the high-level trigger (HLT), consists of a farm of processors running a version of the full event reconstruction software optimized for fast processing, and reduces the event rate to an average of 1 kHz before data storage.

A more detailed description of the CMS detector, together with a definition of the coordinate system used and the relevant kinematic variables, can be found in ref. [1].

3   Event reconstruction

The CMS particle-flow (PF) algorithm [6] aims to reconstruct and identify each individual particle with an optimized combination of information from the various components of the detector. Particles are identified as a mutually exclusive list of PF candidates: charged or neutral hadrons, photons, electrons, or muons. The PF candidates are then used to build higher-level objects, such as jets and p_T^{miss}.

Events are required to have at least one reconstructed vertex. When multiple vertices are reconstructed due to pileup, the vertex with the largest value of summed physics-object p_T^2 is the primary pp interaction vertex (PV).

Photon candidates are reconstructed from energy deposits in the ECAL using algorithms that check the compatibility of the clusters to the size and shape expected from a photon [7]. The identification of the candidates is based on shower-shape and isolation variables [8]. For a photon to be considered isolated, the scalar p_T sum of PF candidates originating from the PV, within a cone of $\Delta R \equiv \sqrt{(\Delta\eta)^2 + (\Delta\phi)^2} < 0.3$ around the photon candidate, is required to be smaller than a given threshold. Only PF candidates that do not overlap with the electromagnetic shower of the candidate photon are included in the isolation sums. The exclusion of PF candidates associated with the photon in the isolation sum, also known as "footprint removal", is significantly improved for the LHC Run 2.

The analyses described in this paper use two sets of photon identification criteria: "loose" and "tight". The loose photon candidates are required to be reconstructed within $|\eta| < 2.5$, whereas tight photon candidates are required to be reconstructed in the ECAL barrel ($|\eta| < 1.44$). Tight photon candidates, used in the performance measurements discussed in section 9, are also required to pass identification and isolation criteria that ensure an efficiency of 80% for the selection of prompt photons and a sample purity of 95%. In the barrel section of the ECAL, an energy resolution of about 1% is achieved for unconverted or late-converting photons in the tens of GeV energy range. The remaining barrel photons have a resolution of about 1.3% up to $|\eta| = 1$, rising to about 2.5% at

$|\eta| = 1.4$. In the endcaps, the resolution of unconverted or late-converting photons is about 2.5%, whereas the remaining endcap photons have a resolution between 3 and 4% [7].

Electrons within the geometrical acceptance $|\eta| < 2.5$ are reconstructed by associating tracks reconstructed in the silicon detector with clusters of energy in the ECAL. Electron candidates are required to satisfy identification criteria [8] based on the shower shape of the energy deposit in the ECAL and the consistency of the electron track with the PV. Electron candidates that are identified as coming from photon conversions in the detector material are removed. The isolation requirement is based on the energy sum of the PF candidates originating from the PV within a cone of $\Delta R < 0.3$ around the electron direction, excluding PF candidates associated to the electron or identified as muons. The mean energy deposited in the isolation cone of the electron from pileup is estimated following the method described in ref. [8] and is subtracted from the isolation sum. Two types of electron identification selection requirements are also used: "loose" and "tight". The loose electrons are selected with an average efficiency of 95% and up to 5% misidentification rate. The loose identification requirements are used in some of the analyses presented in this paper as part of selection requirements designed to remove backgrounds containing electrons e.g. $Z \rightarrow e^+e^-$ events. The tight electrons are selected with an average efficiency of 70% and an average misidentification rate of 1%, and are used to select events used in the performance measurements (section 9).

Muons within the geometrical acceptance $|\eta| < 2.4$ are reconstructed by combining information from the silicon tracker and the muon system [4]. They are required to pass a set of quality criteria based on the number of spatial points measured in the tracker and in the muon system, the fit quality of the muon track and its consistency with the PV. The isolation requirements for muons are based on the energy sum of the PF candidates originating from the PV within a cone of $\Delta R < 0.3$ around the muon direction, excluding PF candidates identified as electrons or muons. The muon isolation variable is corrected for pileup effects from neutral particles by subtracting half of the p_T sum of the charged particles that are inside the isolation cone and not associated with the PV. Two types of muon identification selection requirements are used: "tight" and "loose". The tight muons are selected with an average efficiency of 95% and are used to select the events analyzed in the performance measurement (sections 9 and 10), whereas the loose muons are selected with an average efficiency of 98% and are used when appropriate to veto background events with additional muons. The p_T resolution for muons with $20 < p_T < 100$ GeV is 1% in the barrel and better than 3% in the endcaps. The p_T resolution in the barrel is better than 10% for muons with p_T up to 1 TeV [4].

Hadronically decaying τ lepton candidates detected within $|\eta| < 2.3$ are required to pass identification criteria using the hadron-plus-strips algorithm [9]. The algorithm identifies a jet as a hadronically decaying τ lepton candidate if a subset of the particles assigned to the jet is consistent with the decay products of a τ candidate. In addition, τ candidates are required to be isolated from the surrounding activity in the event. The isolation requirement is computed by summing the p_T of the PF charged and PF photon candidates within an isolation cone of $\Delta R = 0.5$, around the τ candidate direction. A more detailed description of the isolation requirement can be found in ref. [9].

Jets are reconstructed by clustering PF candidates using the infrared- and collinear-safe anti-k_T algorithm [10] with a distance parameter of 0.4. To reduce the effect of pileup collisions, charged PF candidates that originate from pileup vertices are removed [11] before the jet clustering. The jet momentum is determined as the vector sum of all particle momenta in the jet, and is found from simulation to be within 5 to 10% of the true momentum over the full p_T spectrum and detector

acceptance. An energy correction is applied to jet energies to subtract the contribution from pileup. Jet energy corrections, are derived from simulation to adjust the measured jets based on a ratio of the average measured jets to the simulated average jets. Measurements done in situ of the momentum balance in dijet, quantum chromodynamics (QCD) multijet, γ+jet, and leptonic Z+jet events are used to correct for any residual differences in jet energy scale (JES) in data and simulation [11].

Jets originating from the hadronization of bottom (b) quarks are identified ("tagged") via a combined secondary vertex algorithm [12]. The working point of this algorithm provides an average efficiency of $\sim 80\%$ for the identification of jets originating from b quarks whereas the misidentification rate for light quarks or gluons is $\sim 10\%$, and $\sim 40\%$ for charm quarks.

4 Reconstruction and calibration of p_T^{miss}

At hadron colliders, the reconstructed p_T^{miss} is a useful quantity because the net momentum in the plane transverse to the beam is known to be nearly zero from the initial conditions. Therefore, the total p_T of weakly interacting final-state particles can be inferred from the negative vector $\vec{p}_T$ sum of all visible final-state particles. CMS event reconstruction employs two distinct p_T^{miss} reconstruction algorithms, described in the following, both based on PF candidates.

4.1 The p_T^{miss} reconstruction algorithms

The first p_T^{miss} reconstruction algorithm, referred to as PF p_T^{miss} in this paper, defines $\vec{p}_T^{miss}$ as the negative vector p_T sum of all the PF candidates in the event [13, 14]. The PF p_T^{miss} is used in the majority of CMS analyses, since it provides a simple, robust, yet very performant estimate of the p_T^{miss} reconstruction. A second algorithm has been developed to further reduce the dependence on pileup. This algorithm relies on the "pileup per particle identification" (PUPPI) method [15], and uses local shape information around each PF candidate in the event, event pileup properties, and tracking information to reduce the pileup dependence of jet and p_T^{miss} observables.

The PUPPI p_T^{miss} method employs a local shape variable α, which is sensitive to differences between the collinear configuration of particles produced by the hadronization of quarks and gluons produced via QCD mechanisms and the soft diffuse radiation coming from pileup. The α variable is computed for each neutral particle, using the surrounding charged particles compatible with the PV within the tracker acceptance ($|\eta| < 2.5$), and using both charged and neutral particles in the region outside of the tracker coverage. The momenta of the neutral particles are then rescaled according to the probability that they originate from the PV deduced from the local shape variable [15], superseding the need for jet-based pileup corrections [16].

In CMS, the PUPPI algorithm is implemented using PF candidates. A different α definition is adopted for PF candidates within and outside the tracker acceptance. For a given PF candidate i, the α variable is defined as:

$$\alpha_i = \log \sum_{j \neq i, \Delta R_{ij} < 0.4} \left(\frac{p_{Tj}}{\Delta R_{ij}}\right)^2 \begin{cases} \text{for } |\eta_i| < 2.5, & j \text{ are charged PF candidates from PV} \\ \text{for } |\eta_i| > 2.5, & j \text{ are all kinds of reconstructed PF candidates} \end{cases},$$

(4.1)

where j refers to neighboring charged PF candidates originating from the PV within a cone of radius R in η-ϕ space around i, and ΔR_{ij} is the distance in η-ϕ space between the i and j PF candidates.

In addition, charged PF candidates not associated with the PV are used in the calculation if they satisfy $d_z < 0.3\,\mathrm{cm}$, where d_z is the distance in z between the track and the PV. In the absence of tracking coverage, the j in eq. (4.1) extends to all PF candidates within a cone of radius 0.4.

A χ^2 approximation

$$\chi_i^2 = \frac{(\alpha_i - \overline{\alpha}_{\mathrm{PU}})^2}{\mathrm{RMS}_{\mathrm{PU}}^2}, \tag{4.2}$$

is used to determine the likelihood that a PF candidate came from pileup. In this equation, $\overline{\alpha}_{\mathrm{PU}}$ is the median value of the α_i distribution for pileup particles in the event (pileup PF candidates) in the event, and $\mathrm{RMS}_{\mathrm{PU}}$ is the corresponding root-mean-square (RMS) of the α_i distribution. Within the tracker acceptance ($|\eta| < 2.5$), the values of $\overline{\alpha}_{\mathrm{PU}}$ and $\mathrm{RMS}_{\mathrm{PU}}$ are calculated using all charged pileup PF candidates, and are ~ 3.5. Outside the tracker acceptance, the $\overline{\alpha}_{\mathrm{PU}}$ and $\mathrm{RMS}_{\mathrm{PU}}$ are first estimated in the $|\eta| < 2.5$ region and then, with the aid of simulation, are extrapolated in the forward region by means of transfer factors. We define two forward regions: $2.5 < |\eta| < 3$ and $|\eta| > 3$. The typical values of $\overline{\alpha}_{\mathrm{PU}}$ and $\mathrm{RMS}_{\mathrm{PU}}$ in the $2.5 < |\eta| < 3$ region, are ~ 5.5 and ~ 2.5, respectively, whereas in the $|\eta| > 3$ region, are ~ 4.5 and ~ 2, respectively. The χ^2 variable in eq. (4.2) is transformed to a weight using:

$$w_i = F_{\chi^2,\mathrm{NDF}=1}(\chi_i^2), \tag{4.3}$$

where $F_{\chi^2,\mathrm{NDF}=1}$ is the cumulative distribution function, which approximates the χ^2 distribution with one degree of freedom of all PF candidates in the event. The weights range from zero, for PF candidates originating from a pileup vertex, to close to one, for PF candidates originating from the PV. Charged PF candidates associated with the PV take the value of one. Once a weight per PF candidate is determined, the $p_{\mathrm{T}}^{\mathrm{miss}}$ can be computed using the sum of PF candidate four-vectors weighted by their w_i. In addition, the PUPPI-weighted PF candidates can be used as inputs to the jet clustering algorithm. No additional pileup corrections are applied to jets clustered from these weighted inputs. The results presented in this paper are based on jets without PUPPI corrections applied.

The w_i are required to be larger than 0.01 and the minimum scaled p_{T} of neutral PF candidates is required to be $w_i\, p_{\mathrm{T},i} > (A + B\, N_{\mathrm{vtx}})$, where N_{vtx} is the reconstructed vertex multiplicity. In this equation, A and B are adjustable parameters that depend on η. An optimization of the tunable parameters to achieve the best jet p_{T} and $p_{\mathrm{T}}^{\mathrm{miss}}$ resolutions is performed separately for jets in the regions $|\eta| < 2.5$, $2.5 < |\eta| < 3$, and $|\eta| > 3$. The resulting algorithm parameters are similar to those recommended in ref. [15], ranging from 0.2–2.0 and 0.015–0.8, for A and B, respectively.

4.2 Calibration of $p_{\mathrm{T}}^{\mathrm{miss}}$

Examples of sources that can lead to an inaccurate estimation of $p_{\mathrm{T}}^{\mathrm{miss}}$ are the nonlinearity in the calorimeter response to hadrons, the minimum energy thresholds in the calorimeters, and the minimum p_{T} thresholds and inefficiencies in track reconstruction. The estimation of $p_{\mathrm{T}}^{\mathrm{miss}}$ is improved by propagating the correction of the p_{T} of the jets, $\vec{p}_{\mathrm{T, jet}}^{\mathrm{corr}}$, described in ref. [11] to $p_{\mathrm{T}}^{\mathrm{miss}}$ in the following way:

$$\vec{p}_{\mathrm{T}}^{\mathrm{miss}} = \vec{p}_{\mathrm{T}}^{\mathrm{miss, raw}} - \sum_{\mathrm{jets}} (\vec{p}_{\mathrm{T, jet}}^{\mathrm{corr}} - \vec{p}_{\mathrm{T, jet}}), \tag{4.4}$$

where $\vec{p}_{\mathrm{T}}^{\,\mathrm{miss,\,raw}}$ is the uncorrected $p_{\mathrm{T}}^{\mathrm{miss}}$. The sum is over jets with $p_{\mathrm{T}} > 15\,\mathrm{GeV}$. The results in section 9 show that this choice for the jet p_{T} threshold reduces the contribution from jets from pileup interactions and gives a $p_{\mathrm{T}}^{\mathrm{miss}}$ response close to unity.

The corresponding threshold for LHC Run 1, with lower pileup, was 10 GeV [13, 14]. To remove the overlap of jets with electrons and photons, jets with more than 90% of their energy associated to the ECAL are not included in the sum. In addition, if a muon reconstructed using the outer tracking system overlaps with a jet, its four momentum is subtracted from the four momentum of the jet, and the JES correction [11] appropriate for the modified jet momentum is used in the $p_{\mathrm{T}}^{\mathrm{miss}}$ calculation.

The $p_{\mathrm{T}}^{\mathrm{miss}}$ relies on the accurate measurement of the reconstructed physics objects, namely muons, electrons, photons, hadronically decaying taus, jets, and unclustered energy (E_U). The E_U is the contribution from the PF candidates not associated with any of the previous physics objects. Uncertainties related to the $p_{\mathrm{T}}^{\mathrm{miss}}$ measurement depend strongly on the event topology. To estimate the uncertainty in $p_{\mathrm{T}}^{\mathrm{miss}}$, the uncertainty in the momenta of all reconstructed objects is propagated to $p_{\mathrm{T}}^{\mathrm{miss}}$ by varying the estimate of each PF candidate flavor within its uncertainty and recomputing $p_{\mathrm{T}}^{\mathrm{miss}}$.

The JES uncertainties are less than 3% for jets within the tracker acceptance and 1–12% for those outside. The jet energy resolution (JER) uncertainties typically range between 5–20%. The muon energy scale uncertainty is 0.2%, and the electron and photon energy scale uncertainties are 0.6% in the barrel and 1.5% in the endcap. For hadronically decaying τ leptons the energy scale uncertainty is 1.2%. The uncertainties related to the leptons are small, compared to those from the JES and JER uncertainties, and are not considered in the results presented in this paper.

The uncertainty in the E_U for LHC Run 1 was assessed as a uniform 10%, and it accounted for the differences observed between the data and the simulation [14]. The method is improved for LHC Run 2. The E_U uncertainty is evaluated based on the momentum resolution of each PF candidate, which depends on the type of the candidate. A detailed description of the PF candidate calibration can be found in refs. [3, 6, 7]. The p_{T} measurement for PF charged hadrons is dominated by the tracker resolution. For PF neutral hadrons, the p_{T} resolution is dominated by the resolution of the HCAL. The ECAL resolution dominates the PF photon p_{T} measurement, whereas HF intrinsic resolution dominates that for the PF particles in the HF. The largest contributions to the E_U uncertainty are due to the PF neutral hadrons and PF candidates in the HF. Table 1 lists the functional forms of the resolutions of the PF candidate classes contributing to the E_U.

Table 1. Functional forms of the resolutions in the p_{T} measurement for each PF candidate flavor contributing to the E_U [3, 6, 7]. The mathematical symbol $\oplus$ indicates that the quantities are added in quadrature.

PF candidate flavor	Resolution functions
Charged hadron	$(0.00009\,p_{\mathrm{T}})^2 + (0.0085/\sqrt{\sin(2\arctan(\mathrm{e}^{-\eta}))})^2$
Neutral hadron ($|\eta| < 1.3$)	$\min(0.25, (0.8/p_{\mathrm{T}}) \oplus 0.05)$
Neutral hadron ($|\eta| \geq 1.3$)	$\min(0.30, (1/p_{\mathrm{T}}) \oplus 0.04)$
photon	$(0.03/p_{\mathrm{T}}) \oplus 0.001$
HF	$(1./p_{\mathrm{T}}) \oplus 0.05$

5   Simulated events

For comparison with data, simulated Monte Carlo (MC) events are produced for γ+jet and QCD multijet processes at leading order (LO) using the MADGRAPH5_AMC@NLO 2.2.2 [17] generator with up to four additional partons in the matrix element calculations. Samples for the Z+jets and W+jets processes are also produced at next-to-leading order (NLO) using the MADGRAPH5_AMC@NLO generator with up to two additional partons in the matrix element calculations. The $t\bar{t}$ and single top quark background processes are simulated at NLO using POWHEG 2.0 and 1.0, respectively [18, 19]. The diboson samples (WW, WZ, and ZZ) are simulated at NLO using MADGRAPH5_AMC@NLO and POWHEG. A set of triboson samples (WWW, WWZ, WZZ, ZZZ) is simulated at NLO using MADGRAPH5_AMC@NLO. Lastly, the Zγ and Wγ processes, collectively referred to as Vγ in the following, are simulated at LO with MADGRAPH5_AMC@NLO.

The MC samples produced using MADGRAPH5_AMC@NLO and POWHEG generators are interfaced with PYTHIA 8.2 [20] using the CUETP8M1 tune [21] for the fragmentation, hadronization, and underlying event description. For the MADGRAPH5_AMC@NLO samples, jets from the matrix element calculations are matched to the parton shower following the MLM [22] (FxFx [23]) prescription for LO (NLO) samples. The NNPDF3.0 [24] parton distribution functions (PDFs) are used for all samples, with the order matching the matrix element calculations. The simulation of the interactions of all final-state particles with the CMS detector is done with GEANT4 [25]. The simulated events are reconstructed using the same algorithms used for the data. The simulated events include the effects of pileup, with the number of additional pp interactions matching that observed in data. The average number of pileup interactions per proton bunch crossing is 23 for the data sample used in this analysis [26].

6   Event selection

In this paper, several final states are used to evaluate the performance of p_T^{miss} reconstruction algorithms. Monojet and dijet samples are primarily used to study the performance of the algorithms developed to reject spurious events with anomalous p_T^{miss}, and are discussed in section 7. Dilepton and single-photon samples are used to study the p_T^{miss} scale and resolution. A single-lepton sample, which contains events with a genuine p_T^{miss} originating from a neutrino escaping without detection, is used to study the performance of the p_T^{miss} reconstruction algorithm. Finally, the single-lepton and dilepton samples are also used to study the performance of the p_T^{miss} significance. The selection criteria used for each sample are discussed below.

6.1   Monojet and dijet event samples

The events in the monojet sample are selected using triggers with requirements on both $p_{T,\,trig}^{miss}$ and $H_{T,\,trig}^{miss}$, where $p_{T,\,trig}^{miss}$ is the magnitude of the vector $\vec{p}_T$ sum of all PF candidates reconstructed at the trigger level, and $H_{T,\,trig}^{miss}$ is the magnitude of the vector $\vec{p}_T$ sum of jets with $p_T > 20\,\text{GeV}$ and $|\eta| < 5.0$ reconstructed at the trigger level. Candidate events are required to have $p_T^{miss} > 250\,\text{GeV}$, and the highest p_T (leading) jet in the event is required to have $p_T > 100\,\text{GeV}$ and $|\eta| < 2.4$. The background from processes including W bosons decaying leptonically is suppressed by imposing a veto on events containing one or more loose muons or electrons with $p_T > 10\,\text{GeV}$, or τ leptons

with $p_T > 18$ GeV. Events that contain a loose, isolated photon with $p_T > 15$ GeV and $|\eta| < 2.5$ are also vetoed. This helps suppress electroweak (EW) backgrounds with a photon radiated from an initial state parton. To reduce the contamination from top quark backgrounds, events are rejected if they contain a b-tagged jet with $p_T > 20$ GeV and $|\eta| < 2.4$.

The QCD multijet background with p_T^{miss} arising from mismeasurements of jet momenta is suppressed by requiring the angle between the $\vec{p}_T^{miss}$ direction and each of the first four leading jets with $p_T > 30$ GeV is at least 0.5 radians. This selection facilitates the study of sources that could lead to artificially large ("spurious") p_T^{miss} due a malfunctioning detector (section 7).

The events in the dijet sample are also selected using the $p_{T, trig}^{miss}$ and $H_{T, trig}^{miss}$ triggers. Candidate events are required to have p_T^{miss} greater than 250 GeV and the leading (subleading) jet in the event is required to have $p_T > 500$ (200) GeV. As for the monojet sample, events with an identified loose lepton, photon, or a b-tagged jet are rejected.

6.2 Dilepton event samples

The dilepton samples are subdivided into two categories based on the flavor of the lepton, namely $Z \to \mu^+\mu^-$ and $Z \to e^+e^-$. The events for the $Z \to \mu^+\mu^-$ sample are recorded using dimuon triggers that select events where the p_T of each of the two leading muons is above an asymmetric threshold. Candidate events are required to have both the leading (subleading) muon p_T greater than 25 (20) GeV and an invariant mass in the range of 80 to 100 GeV, compatible with the mass of the Z boson [27]. Events are vetoed if there is an additional muon or electron with $p_T > 20$ GeV. The events in the $Z \to e^+e^-$ samples are recorded using dielectron triggers that have asymmetric selection requirements on the p_T of the two leading electrons. Candidate events are required to have the leading (subleading) electron p_T greater than 25 (20) GeV . As in the dimuon case, the invariant mass of the dielectron system is required to be in the range of 80 to 100 GeV . Events are vetoed if there is an additional muon or electron with $p_T > 20$ GeV. The spectrum of the Z boson transverse momentum, q_T, is shown in figure 1 where only the statistical uncertainty in the simulated samples is considered because the dilepton energy resolution is very good.

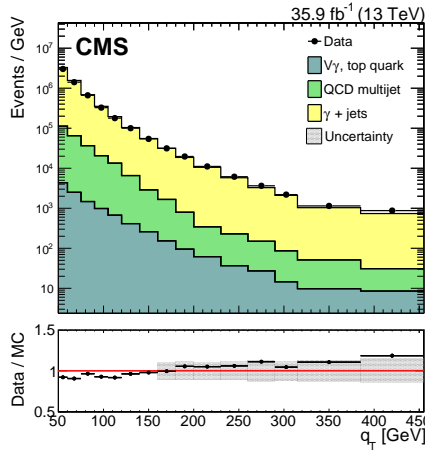## 6.3 Single-photon event sample

The events in the single-photon sample are selected using a set of isolated single-photon triggers with varying thresholds. The p_T thresholds of the triggers are 30, 50, 75, 90, 120, and 165 GeV. The first five of these triggers used different, luminosity dependent, L1 accept rates (prescales) during the data-taking periods. Candidate events are weighted based on the prescale values of the triggers.

Candidate events are required to have a tight photon with $p_T > 50$ GeV. To match the trigger conditions, the leading photon is further required to have the ratio of the energy deposited in a 3×3 crystal region of the ECAL, which is centered around the crystal containing an energy deposit greater than all of its immediate neighbors, to the energy of the entire deposit of the photon greater than 0.9.

The single-photon sample events are also required to have at least one jet with p_T greater than 40 GeV, and events with leptons with p_T greater than 20 GeV are vetoed. The photon q_T spectrum is shown in figure 2. As in figure 1, only the statistical uncertainty in the simulated samples is considered because the photon energy resolution is very good.
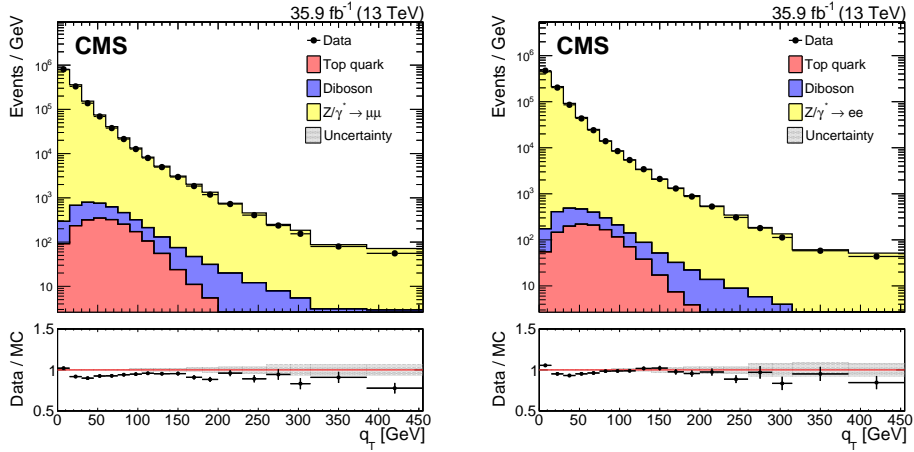
Figure 1. Upper panels: distributions of Z boson q_T in $Z \rightarrow \mu^+\mu^-$ (left) and $Z \rightarrow e^+e^-$ (right) samples. The diboson contribution corresponds to processes with two electroweak bosons produced in the final state. The top quark contribution corresponds to the top pair and single top production processes. The last bin includes all events with $q_T > 385\,\text{GeV}$. Lower panel: data to simulation ratio. The band corresponds to the statistical uncertainty in simulated samples.

Figure 2. Upper panel: distribution of the photon q_T in the single-photon sample. The $V\gamma$, top quark contribution corresponds to the $Z\gamma$, $W\gamma$, top pair and single top production processes. The last bin includes all events with $q_T > 385\,\text{GeV}$. Lower panel: data to simulation ratio. The band corresponds to the statistical uncertainty in the simulated samples.

6.4   Single-lepton event samples

The single-lepton samples are subdivided into two categories based on the flavor of the lepton. These events in the single-muon (single-electron) sample are selected using triggers based on the p_T and the isolation of the muon (electron). Candidate events are required to have a tight muon (electron) with p_T greater than 25 (26) GeV . Events with an additional lepton with p_T greater than 10 GeV, or with a b-tagged jet, are rejected.

These single-lepton samples consist mainly of W+jets events. One source of background stems from QCD multijet events containing a jet misidentified as a lepton. The simulation indicates that

the magnitude of this background is small. However, since the uncertainties in simulating this background can be significant, we use a data control region to estimate it. The data control sample is selected by inverting the requirement on the relative isolation of the lepton and is dominated by QCD multijet events. The normalization of this background is then corrected by comparing the observed and expected number of events in the data control sample. Other processes are estimated from simulation.

The spectrum of the W boson transverse momentum q_T is shown in figure 3. In contrast to figures 1 and 2, the effects of the systematic uncertainties from the JES, JER, and E_U are sizable and are included in addition to the systematic uncertainty from the limited statistics in the simulated samples.
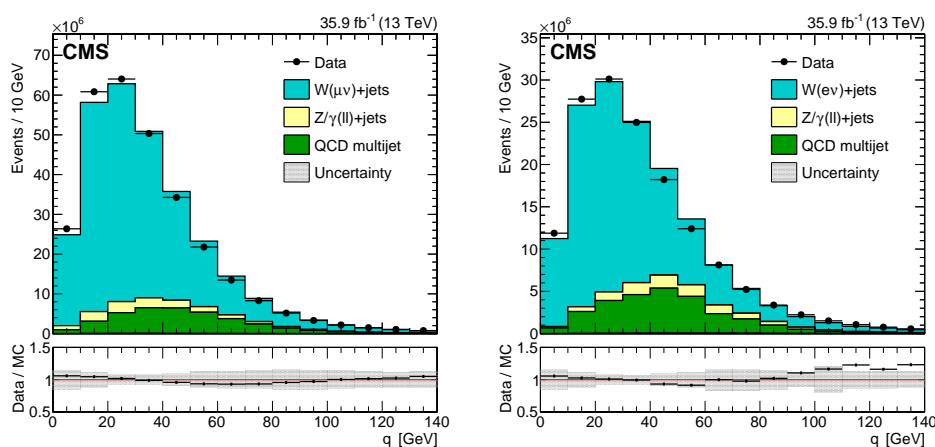
Figure 3. Upper panels: distributions of W boson q_T in single-muon (left) and single-electron (right) samples. The last bin includes all events with $q_T > 130$ GeV. Lower panels: data to simulation ratio. The systematic uncertainties due to the JES, the JER, and variations in the E_U are added in quadrature and displayed with a band.

7 Anomalous p_T^{miss} events

Anomalous high-p_T^{miss} events can arise because of a variety of reconstruction failures or malfunctioning detectors. In the ECAL, spurious deposits may appear due to noisy sensors in the ECAL photodetectors, or from genuine showers with noncollision origins, such as those caused by the production of muons when beam protons undergo collisions upstream of the detector (beam halo). An additional source of artificial p_T^{miss} is the presence of dead cells, leading to underestimation of the energy. In the HCAL, spurious energy can arise from noise in the hybrid photodiode (HPD) and in the readout box (RBX) electronics, as well as from direct particle interactions with the light guides and photomultiplier tubes of the HF. These sources have been studied extensively in the data collected in LHC Run 1 [13, 14]. Algorithms (filters) developed during LHC Run 1 to identify and suppress events with anomalously high p_T^{miss} are also used for this data (LHC Run 2) with the necessary modifications for the upgraded detector [28] and the different data-taking conditions. An additional set of filters was also developed during this run to identify new sources of artificial p_T^{miss}. Details of the various filters are given below.

- **HCAL filters**

  The geometrical patterns of HPD or RBX channels as well as the pulse shape and timing information are used by various HCAL barrel and endcap (HBHE) algorithms to identify and eliminate noise. These filter algorithms operate both in "noise filtering" and "event filtering" modes. In the noise filtering mode, the anomalous energy deposits are removed from the event reconstruction; in the filtering mode, the event is removed from the data set. In addition, there is an isolation-based noise filter that utilizes a topological algorithm, where energy deposits in HCAL and ECAL are combined and compared with measurements from the tracker to identify isolated anomalous activity in HB/HE. An additional noise filter based on pulse shapes uses information at the cluster reconstruction level and searches for uncharacteristic noise signals in the HB/HE HPD channels. It relies on the known pulse shapes of HPDs, and is similar the RBX pulse shape filters [29], but explicitly corrects for the presence of in-time and out-of-time pileup when testing for anomalous pulse shapes.

- **ECAL filters**

  For the ECAL, much of the electronics noise and spurious signals from particle interactions with the photodetectors is removed during reconstruction using the topological and timing information. The remaining effects that lead to high-$p_\mathrm{T}^\mathrm{miss}$ signatures, such as anomalously high energy deposits in supercrystals, and the lack of information for channels that have nonfunctioning readout electronics, are removed through dedicated noise filters.

  During this data-taking run (LHC Run 2), five ECAL endcap supercrystals produced large, anomalous pulses, leading to spurious $p_\mathrm{T}^\mathrm{miss}$. These crystals are removed from the readout, and their energies are not considered. Furthermore, in about 0.7% of ECAL towers (i.e. 5×5 ECAL crystals), the crystal-by-crystal information is not available. The trigger primitive (TP) [5] information, however, is still available, and is used to estimate the energy. The TP information saturates above 127.5 GeV . Events with a TP close to saturation in any of these ECAL towers are removed.

- **Beam halo filter**

  Machine-induced backgrounds, especially beam halo, can cause anomalously large $p_\mathrm{T}^\mathrm{miss}$. Beam halo particles travel nearly parallel to the collision axis and can sometimes interact in the calorimeters, leaving energy deposits along a line with constant ϕ. In addition, interactions in the CSC, a subdetector with good reconstruction performance for both collision and noncollision muons, will often be in line with the calorimeter deposits. The beam halo filter was redesigned for LHC Run 2. In LHC Run 1 the filter was based solely on information from the CSC. However, the LHC Run 2 filter exploits information from both the CSC and the calorimeters, resulting in a significant improvement in performance.

- **Reconstruction filters**

  An additional source of anomalous high-$p_\mathrm{T}^\mathrm{miss}$ events during LHC Run 2 was poor reconstruction of muons during the muon-tracking iteration step [4]. If a high-p_T track has a low quality reconstruction, it could contribute to $p_\mathrm{T}^\mathrm{miss}$ either as a poorly reconstructed PF muon, or as a poorly reconstructed PF charged hadron. The poorly reconstructed muons and

charged hadrons are identified based on the ratio of the relative p_T uncertainty of the track p_T, determined by the Tune-P algorithm [4], or the inner track p_T. Once a poorly reconstructed muon or a charged hadron is identified, dedicated filters are designed to reject these events.

Figure 4 shows a comparison of the p_T^{miss} (left) and jet ϕ (right) distributions before and after the application of the event filters for the dijet and monojet samples, respectively. The anomalous events with large p_T^{miss} in the dijet sample are mostly due to electronic noise in the calorimeters. The jet ϕ distribution in the monojet sample is used to validate the performance of the beam halo filter. The angular distribution of beam halo events is dictated by the shape of the LHC tunnel and the beamline elements [30] and results in an excess of events with jet $\phi \approx 0$ or $\phi \approx \pi$. These events are removed by the beam halo filter. In both samples, the simulated p_T^{miss} and jet ϕ distributions are in good agreement with data after the application of all the filters. The event filters are designed to identify more than 85–90% of the spurious high-p_T^{miss} events with a mistag rate of less than 0.1%. In addition to the event filtering algorithms, a jet identification selection is imposed, which requires the neutral hadron energy fraction of a jet be less than 0.9. This selection rejects more than 99% of the noise jets, independent of jet p_T, with a negligible mistag rate.
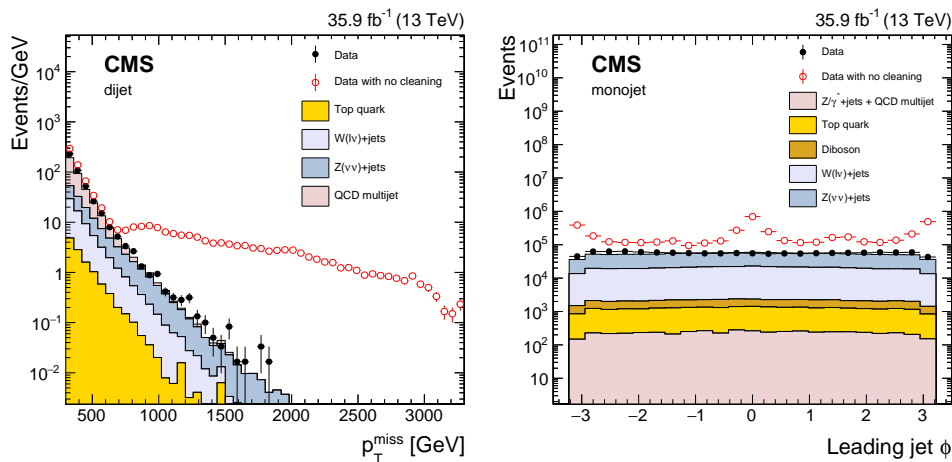
Figure 4. The p_T^{miss} (left) and jet ϕ (right) distributions for events passing the dijet (left) and monojet (right) selection with the event filtering algorithms applied, including that based on jet identification requirements (filled markers), without the event filtering algorithms applied (open markers), and from simulation (solid histograms).

8 Performance of p_T^{miss} reconstruction at the trigger level

At L1, p_T^{miss} is computed at the global calorimeter trigger (GCT) level [5], which is the last stage of the L1 calorimeter trigger chain. The trigger-level quantities computed by the GCT use data from the regional calorimeter trigger (RCT) [5], which receives the transverse energies, E_T, and quality flags from ECAL and HCAL. At GCT level, the p_T^{miss} is calculated by summing the regional transverse energy values and rotating the resulting vector by 180°. A more detailed description can be found in [5]. Although the RCT coverage could be extended to $|\eta|$ of 5.0, the p_T^{miss} algorithm at L1 only uses information from trigger towers within $|\eta| < 3.0$, due to the bandwidth restrictions of the trigger system.

Two reconstruction algorithms are used at the HLT. A p_T^{miss} variable using only information from the calorimeters (Calo p_T^{miss}) is used as a prefilter to a more complex, PF-based p_T^{miss} reconstruction. The Calo p_T^{miss} is computed by taking the negative vector E_T sum of all calorimeter towers, whereas PF p_T^{miss} is based on the negative vector p_T sum of all reconstructed PF jets without a p_T requirement, as in the case of the offline reconstruction algorithms.

To maintain the lowest possible thresholds for the p_T^{miss} triggers, event filtering algorithms are applied at the trigger level. In contrast to the offline case, at the trigger level the calorimeter energy deposits flagged as being consistent either with HB/HE noise or beam halo are removed from the energy sum, and p_T^{miss} is recomputed. The noise filtering algorithms used at the HLT are fully efficient with respect to the offline filtering algorithms, and reduce the rate of p_T^{miss} triggers by up to a factor of 2.5, depending on the p_T^{miss} threshold.

As with the offline reconstruction, HLT PF p_T^{miss} is calibrated by correcting the p_T of the jets using the jet energy corrections. In contrast to the offline calibration, the corrections for the jets are only propagated to the p_T^{miss} if the jet p_T is above 35 GeV . The performance of the p_T^{miss} triggers is measured in single-electron samples. The efficiency for each trigger-level p_T^{miss} object type is shown in figure 5. The calibrated p_T^{miss} at the HLT level yields an improved efficiency at lower p_T. As a result, online trigger thresholds are set to higher values, typically $\gtrsim$170 GeV, yielding the same performance offline, for up to 10% rate reduction depending on the p_T^{miss} threshold.
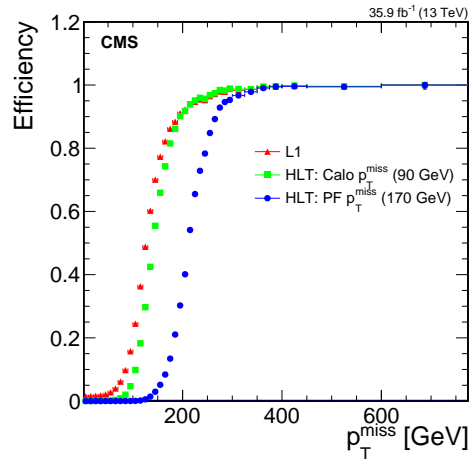
Figure 5. The p_T^{miss} trigger efficiency as a function of offline p_T^{miss}, measured using a single-electron sample. The efficiency of each reconstruction algorithm, namely the L1, the calorimeter, and the PF-based p_T^{miss} algorithms, is shown separately. The numbers in parentheses correspond to the HLT p_T^{miss} thresholds. The logical OR of the L1 p_T^{miss} triggers with requirements on p_T^{miss} greater than 50, 60, 70, 80, 90, 100 and 120 GeV are used.

9   Performance of p_T^{miss} algorithms

A well-measured Z/γ boson provides a unique event axis and a precise momentum scale. To this end, the response and resolution of p_T^{miss} is studied in samples with an identified Z boson decaying to a pair of electrons or muons, or with an isolated photon. Such events should have little or no genuine p_T^{miss}, and the performance is measured by comparing the momenta of the vector boson to

that of the hadronic recoil system. The hadronic recoil system is defined as the vector p_T sum of all PF candidates except for the vector boson (or its decay products in the case of the Z boson decay). In figure 6 the kinematic representations of the transverse momenta of the vector boson and the hadronic recoil, $\vec{q}_T$ and $\vec{u}_T$, are shown. Momentum conservation in the transverse plane imposes $\vec{q}_T + \vec{u}_T + \vec{p}_T^{\,\text{miss}} = 0$.
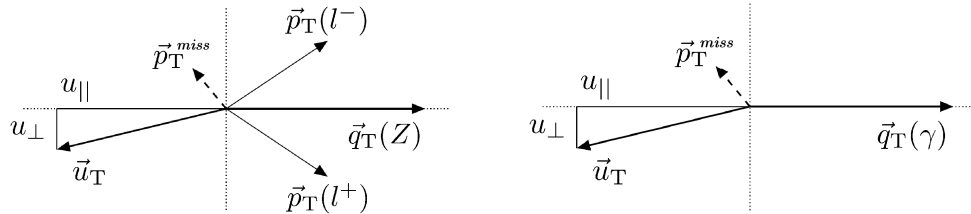
Figure 6. Illustration of the Z boson (left) and photon (right) event kinematics in the transverse plane. The vector $\vec{u}_T$ denotes the vectorial sum of all particles reconstructed in the event except for the two leptons from the Z decay (left) or the photon (right).

The components of the hadronic recoil parallel and perpendicular to the boson axis are denoted by $u_\parallel$ and $u_\perp$, respectively. These are used to study the p_T^{miss} response and resolution. Specifically, the mean of the distribution of the magnitude of $\vec{u}_\parallel + \vec{q}_\perp$, denoted as $u_\parallel + q_T$, is used to estimate the p_T^{miss} response, whereas the RMS of the $u_\parallel + q_T$ and $u_\perp$ distributions are used to estimate the resolution of $u_\parallel$ and $u_\perp$, denoted by $\sigma(u_\parallel)$ and $\sigma(u_\perp)$, respectively. The response of p_T^{miss} is defined as $-\langle u_\parallel \rangle / \langle q_T \rangle$ where $\langle \, \rangle$ indicates the mean of the distributions.

An alternative method insensitive to tails in the distributions is also used. The $u_\parallel + q_T$ and $u_\perp$ are parametrized using a Voigtian function, defined as the convolution of a Breit-Wigner and a Gaussian distribution. The results obtained with the alternative method agree within 2% with those obtained using the primary method (i.e., mean/RMS), indicating that the effect of the nonGaussian tails on the p_T^{miss} performance is small. In the following sections, the performance of the PF and PUPPI p_T^{miss} algorithms is shown using the primary method.

9.1 Performance of the PF p_T^{miss} algorithm

The PF p_T^{miss} distributions in dilepton and photon samples are shown in figure 7. The data distributions are modeled well by the simulation.

The p_T^{miss} resolution in these events is dominated by the resolution of the hadronic activity, since the momentum resolution for leptons and photons is $\sigma_{p_T}/p_T \lesssim 1.5\%$ [4, 7], compared to 5–20% for the jet momentum resolution [11]. The uncertainty shown in the figures includes uncertainties in the JES, the JER, and the energy scale of unclustered particles, added in quadrature. The increase in the uncertainty band around 40 GeV is related to the JES and the JER sources in events with at least one jet and no genuine p_T^{miss}. For higher values of p_T^{miss}, where processes with genuine p_T^{miss}, e.g., top quark background, are present, the uncertainty is somewhat smaller.

Distributions of $u_\parallel + q_T$ and $u_\perp$ in $Z \to \mu^+\mu^-$, $Z \to e^+e^-$ and γ+jets events are shown in figure 8. The kinematic definition of $u_\parallel$ dictates that for processes with no genuine p_T^{miss}, $u_\parallel$ is balanced with the boson q_T. Therefore, the vectorial sum of $u_\parallel$ and q_T results in a symmetric distribution, centered at zero; any deviations from this behavior imply imperfect calibration of p_T^{miss}.
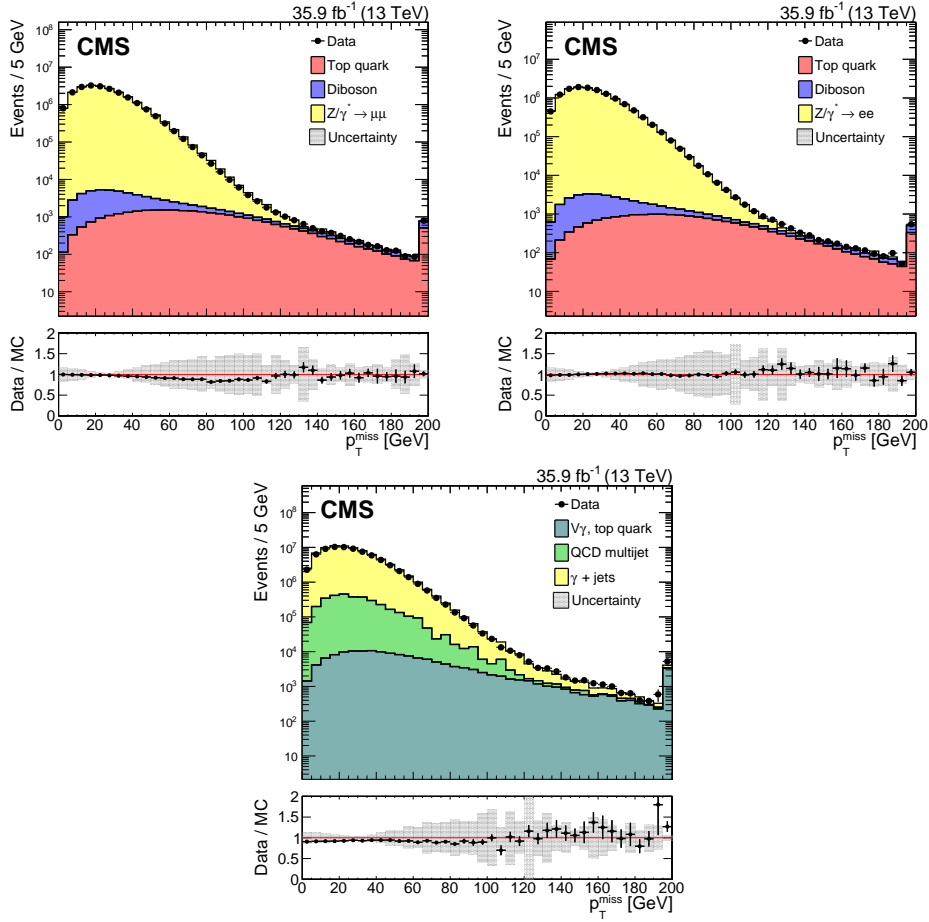
Figure 7. Upper panel: distributions of p_T^{miss} in $Z \to \mu^+\mu^-$ (top left), $Z \to e^+e^-$ (top right), and γ+jets events (lower middle) in data and simulation. The last bin includes all events with $p_T^{miss} > 195$ GeV. Lower panel: data to simulation ratio. The systematic uncertainties due to the JES, the JER, and variations in the E_U are added in quadrature and represented by the shaded band.

Events with genuine p_T^{miss} due to the presence of neutrinos, $u_\parallel$ and q_T are not balanced, leading to an asymmetric distribution. The $u_\perp$ distribution is symmetric with a mean value of zero. This symmetry is due to the assumed isotropic nature of the energy fluctuations of the detector noise and underlying event. Good agreement is observed between data and simulation for all the distributions.

Figure 9 shows the p_T^{miss} response as a function of q_T, in data and simulation, in $Z \to \mu^+\mu^-$, $Z \to e^+e^-$, and photon events. The response reaches unity for boson $p_T > 100$ GeV. Deviations from unity indicate imperfect calibration of the hadronic energy scale. The underestimation of the hadronic response observed at smaller $q_T \lesssim 100$ GeV is due to the significant contribution of the uncalibrated component of p_T^{miss}, which mainly consists of jets with $p_T < 15$ GeV and unclustered particles. There is no dedicated response correction for the E_U. The response of p_T^{miss} agrees for all three samples within 2%; a significant improvement with respect to the results from the LHC Run 1 [13, 14]. The "footprint removal" discussed in section 3 plays an important role in this improvement. The residual response difference among the samples stems from the different mechanism used to differentiate muons, electrons, and photons from jets used in the correction of
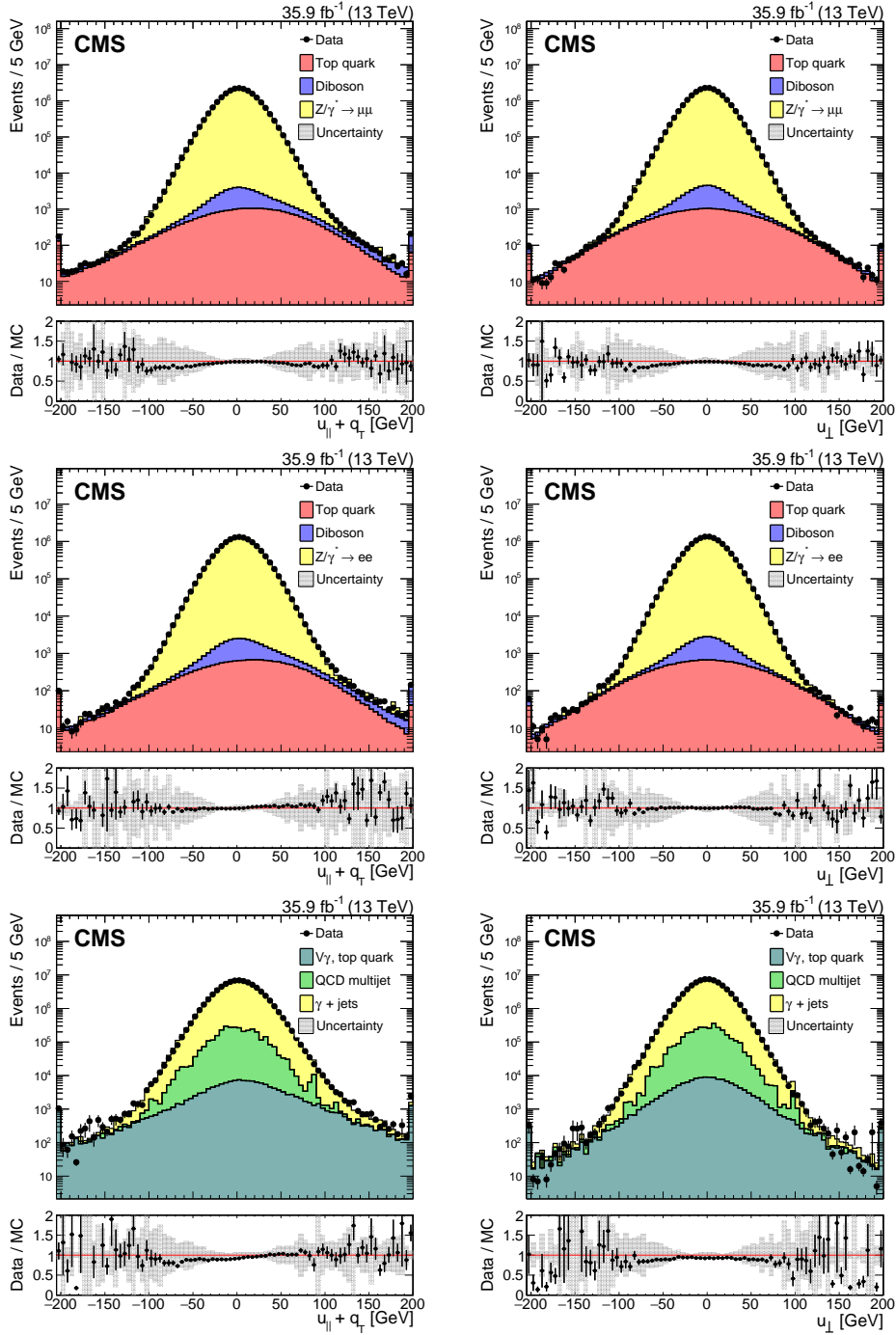
Figure 8. Distribution of $u_{\parallel}+q_T$ and $u_{\perp}$ components of the hadronic recoil, in data (filled markers) and simulation (solid histograms), in the $Z \to \mu^+\mu^-$ (upper), $Z \to e^+e^-$ (middle), and γ+jets (lower) samples. The first and the last bins include all events below -195 and above $+195$, respectively. The points in the lower panel of each plot show the data to simulation ratio. The systematic uncertainties due to the JES, the JER, and variations in the E_U are added in quadrature and represented by the shaded band.

the p_T^{miss}, as discussed in section 4.2. Simulation studies have shown that in the case of electrons and photons, a small fraction ($\lesssim 10\%$) of jets survive the differentiation criteria yet overlap with prompt electrons and photons. As a result, these jets wrongly contribute to the p_T^{miss} calibration, leading to a 1–2% lower response in the electron and photon channels. Future studies will aim at further improving the electron/photon and jet differentiation mechanism. Overall, we observe good agreement between data and simulation.
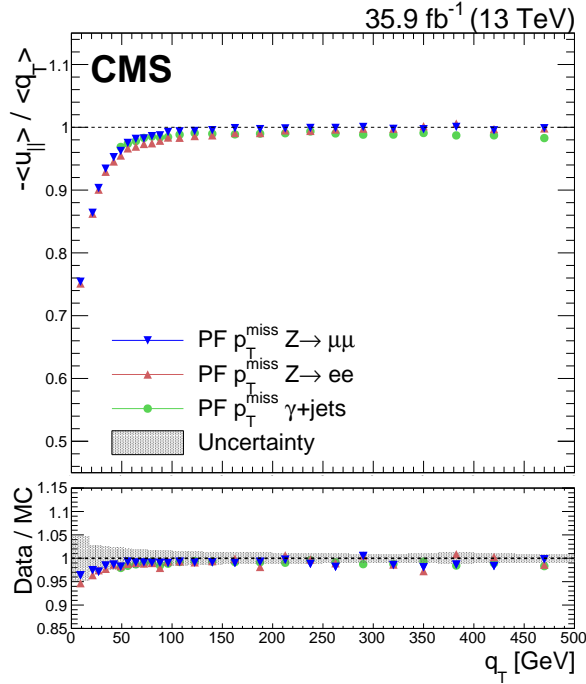
Figure 9. Upper panel: response of p_T^{miss}, defined as $-\langle u_{\parallel} \rangle / \langle q_T \rangle$, in data in $Z \to \mu^+\mu^-$ (blue), $Z \to e^+e^-$ (red), and γ+jets (green) events. Lower panel: ratio of the p_T^{miss} response in data and simulation. The band corresponds to the systematic uncertainties due to the JES, the JER, and variations in the E_U added in quadrature, estimated from the $Z \to e^+e^-$ sample.

The resolution of p_T^{miss} for the $u_{\parallel}$ and $u_{\perp}$ components of the hadronic recoil as a function of q_T is shown in figure 10 (upper row). To compare the resolution of p_T^{miss} consistently across the samples, the resolution in each sample is corrected for the differences observed in the response. The correction has a negligible impact on the results. The resolutions measured in different samples are in good agreement. The relative resolution, both in $u_{\parallel}$ and $u_{\perp}$, improves as a function of q_T because of the improved energy resolution in the calorimeters. Furthermore, due to the isotropic nature of energy fluctuations stemming from detector noise and the underlying event, the dependence of the resolution of $u_{\perp}$ on q_T is smaller than for $u_{\parallel}$. For $q_T > 200\,\text{GeV}$, the p_T^{miss} resolution is $\approx 13\%$ and $\approx 9\%$, for $u_{\parallel}$ and $u_{\perp}$, respectively.

The resolution of the $u_{\parallel}$ and $u_{\perp}$ components of the hadronic recoil as a function of N_{vtx}, are shown in figure 10 (middle row). The resolutions measured in different samples, and in data and simulation, are in good agreement. However, the resolution shows strong dependence on N_{vtx}, since pileup mitigation techniques are employed only for the PF jets, but not for the PF p_T^{miss} algorithm.

The resolution is parametrized as a function of N_{vtx}:

$$f(N_{vtx}) = \sqrt{\sigma_c^2 + \frac{N_{vtx}}{0.70}\sigma_{PU^2}}, \tag{9.1}$$

where σ_c is the resolution term induced by the hard scattering interaction and σ_{PU} is the average contribution to the resolution from each additional pileup interaction. The factor 0.70 accounts for the vertex reconstruction efficiency [31]. Results of the parametrization for the $u_\parallel$ and $u_\perp$ components are given in table 2. Good agreement is observed between data and simulation and no additional corrections are used for the p_T^{miss} calibration. Every additional pileup vertex degrades the resolution of each component by 3.8–4.0 GeV .

Lastly, figure 10 (lower row) shows an alternative parametrization of the resolution of $u_\parallel$ and $u_\perp$ as a function of the scalar p_T sum of all PF candidates ($\sum E_T$). The resolutions measured in different samples, and in data and simulation, are in good agreement. The relative p_T^{miss} resolution improves with increasing $\sum E_T$, driven by the amount of the activity in the calorimeters. The resolution in different samples is parametrized as:

$$f\left(\sum E_T\right) = \sigma_0 + \sigma_s\sqrt{\sum E_T}, \tag{9.2}$$

where σ_0 is the resolution term induced by intrinsic detector noise and σ_s is the stochastic resolution term. Results of the parametrization for the $u_\parallel$ and $u_\perp$ components are given in table 3. The results are found to be consistent between data and simulation and no additional corrections are used for the p_T^{miss} calibration.

**Table 2**. Parametrization results of the resolution curves for the $u_\parallel$ and $u_\perp$ components as a function of N_{vtx}. The parameter values for σ_c are obtained from data and simulation, and the values for σ_{PU} are obtained from data, along with a ratio R_{PU} of data and simulation. The uncertainties displayed for both components are obtained from the fit, and for simulation the JES, the JER, and E_U uncertainties are added in quadrature.

Process	σ_c(data)[GeV]	σ_c(MC)[GeV]	σ_{PU}(data)[GeV]	$R_{PU} = \sigma_{PU}$(data)$/\sigma_{PU}$(MC)
		$u_\parallel$ component		
$Z \to \mu^+\mu^-$	13.9 ± 0.07	11.9 ± 1.53	3.82 ± 0.01	0.95 ± 0.04
$Z \to e^+e^-$	14.6 ± 0.09	12.0 ± 1.09	3.80 ± 0.02	0.95 ± 0.03
γ+jets	12.2 ± 0.10	10.2 ± 1.98	3.97 ± 0.02	0.97 ± 0.05
		$u_\perp$ component		
$Z \to \mu^+\mu^-$	10.3 ± 0.08	8.58 ± 2.20	3.87 ± 0.01	0.97 ± 0.04
$Z \to e^+e^-$	10.7 ± 0.10	8.71 ± 1.76	3.89 ± 0.01	0.96 ± 0.03
γ+jets	9.04 ± 0.11	6.93 ± 2.70	3.94 ± 0.01	0.97 ± 0.04
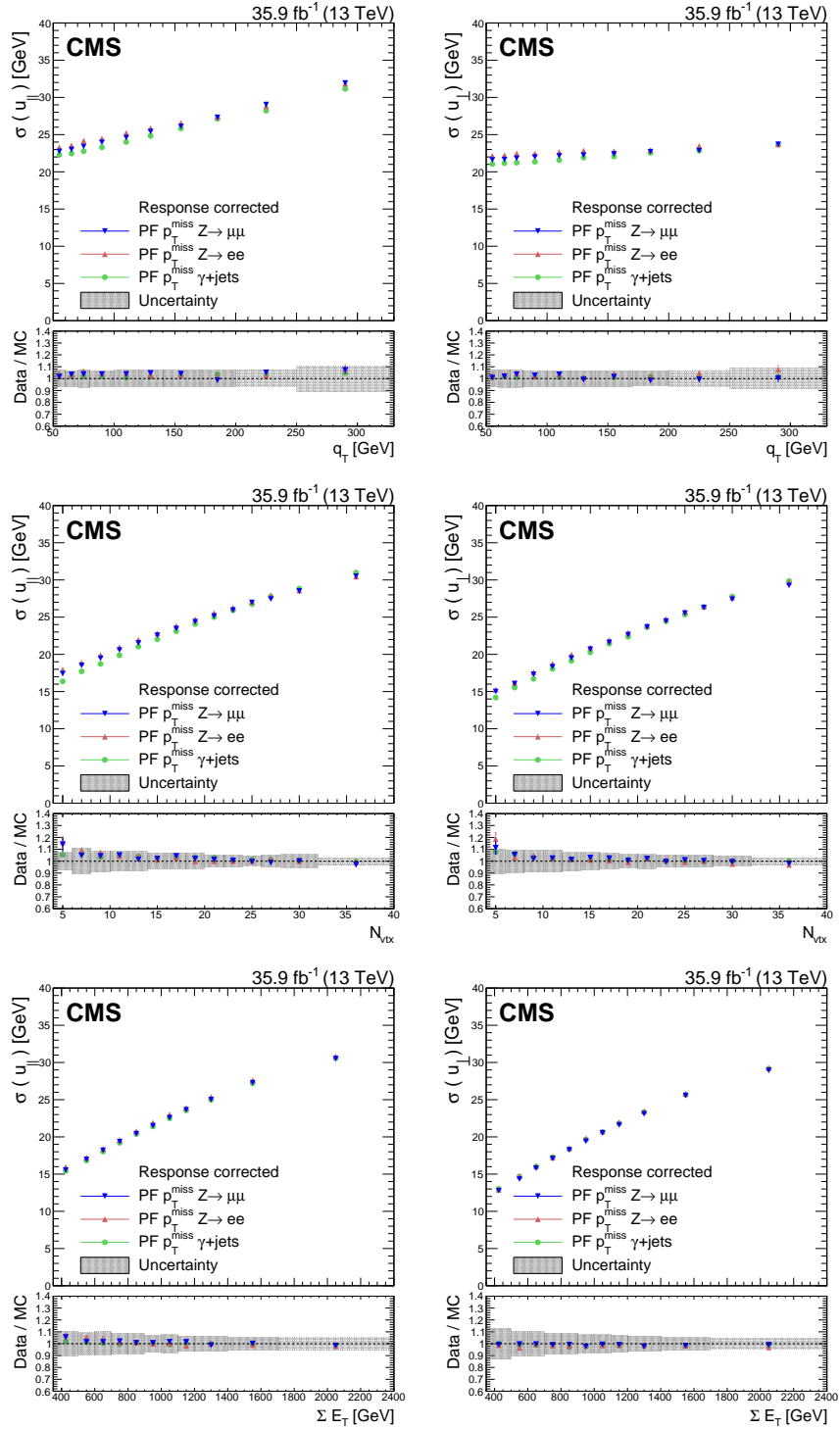
Figure 10. Resolution of the $u_\parallel$ and $u_\perp$ components of the hadronic recoil as a function of q_T (upper row), the reconstructed vertices (middle row), and the scalar p_T sum of all PF candidates (lower row), in $Z \to \mu^+\mu^-$, $Z \to e^+e^-$, and γ+jets events. In each plot, the upper panel shows the resolution in data, whereas the lower panel shows the ratio of data to simulation. The band corresponds to the systematic uncertainties due to the JES, the JER, and variations in the E_U added in quadrature, estimated from the $Z \to e^+e^-$ sample.

Table 3. Parametrization results of the resolution curves for $u_\parallel$ and $u_\perp$ components as a function of the scalar p_T sum of all PF candidates. The parameter values for σ_0 are obtained from data and simulation, whereas the σ_s are obtained from data along with the ratio R_s, the ratio of data and simulation. The uncertainties displayed for both components are obtained from the fit, and for simulation the JES, the JER, and E_U uncertainties are added in quadrature.

Process	σ_0(data)[GeV]	σ_0(MC)[GeV]	σ_s[GeV$^{1/2}$]	$R_s = \sigma_s$(data)/σ_s(MC)
		$u_\parallel$ component		
$Z \to \mu^+\mu^-$	1.98 ± 0.07	0.85 ± 2.45	0.64 ± 0.01	0.95 ± 0.11
$Z \to e^+e^-$	2.18 ± 0.09	0.19 ± 2.90	0.64 ± 0.01	0.92 ± 0.11
γ+jets	1.85 ± 0.09	0.94 ± 2.52	0.64 ± 0.01	0.96 ± 0.11
		$u_\perp$ component		
$Z \to \mu^+\mu^-$	-1.63 ± 0.06	-1.72 ± 2.53	0.68 ± 0.01	0.99 ± 0.11
$Z \to e^+e^-$	-1.42 ± 0.08	-1.98 ± 2.95	0.69 ± 0.01	0.96 ± 0.12
γ+jets	-1.16 ± 0.08	-1.31 ± 2.53	0.68 ± 0.01	0.98 ± 0.11

9.2 Performance of the PUPPI p_T^{miss} algorithm

The PUPPI p_T^{miss} distributions in the dilepton samples are shown in figure 11. The data distributions are modeled well by the simulation, in both the muon and the electron channels. As in the case of PF p_T^{miss}, the p_T^{miss} resolution in these events is dominated by the resolution of the hadronic activity, but the PUPPI-weighted PF candidates yield improved resolution for jets compared to the PF case. This is also reflected in the uncertainty shown in the figures, which includes the uncertainties due to JES and JER, and the energy scale of the unclustered particles.
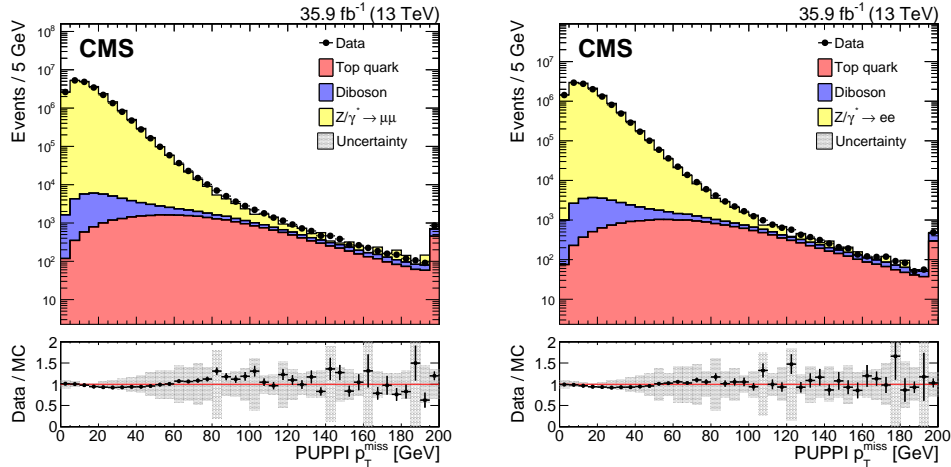
Figure 11. Upper panels: distributions of PUPPI p_T^{miss} in $Z \to \mu^+\mu^-$ (left) and $Z \to e^+e^-$ (right) events. The last bin includes all events with $p_T^{miss} > 195$ GeV. Lower panels: data-to-simulation ratio. The band corresponds to the systematic uncertainties due to the JES, the JER, and variations in the E_U added in quadrature, estimated from the $Z \to e^+e^-$ sample.

The distributions in $Z \rightarrow \mu^+\mu^-$ and $Z \rightarrow e^+e^-$ events of the vectorial sum $u_\parallel + q_T$ and of $u_\perp$ using PUPPI p_T^{miss}, are shown in figure 12. Following the same arguments as in the PF p_T^{miss} case, in events with no genuine p_T^{miss} the vectorial sum of $u_\parallel$ and q_T is symmetric around zero, whereas for processes with genuine p_T^{miss} an asymmetric behavior is observed. The distribution of $u_\perp$ is symmetric around zero. Simulation describes data well for all distributions.
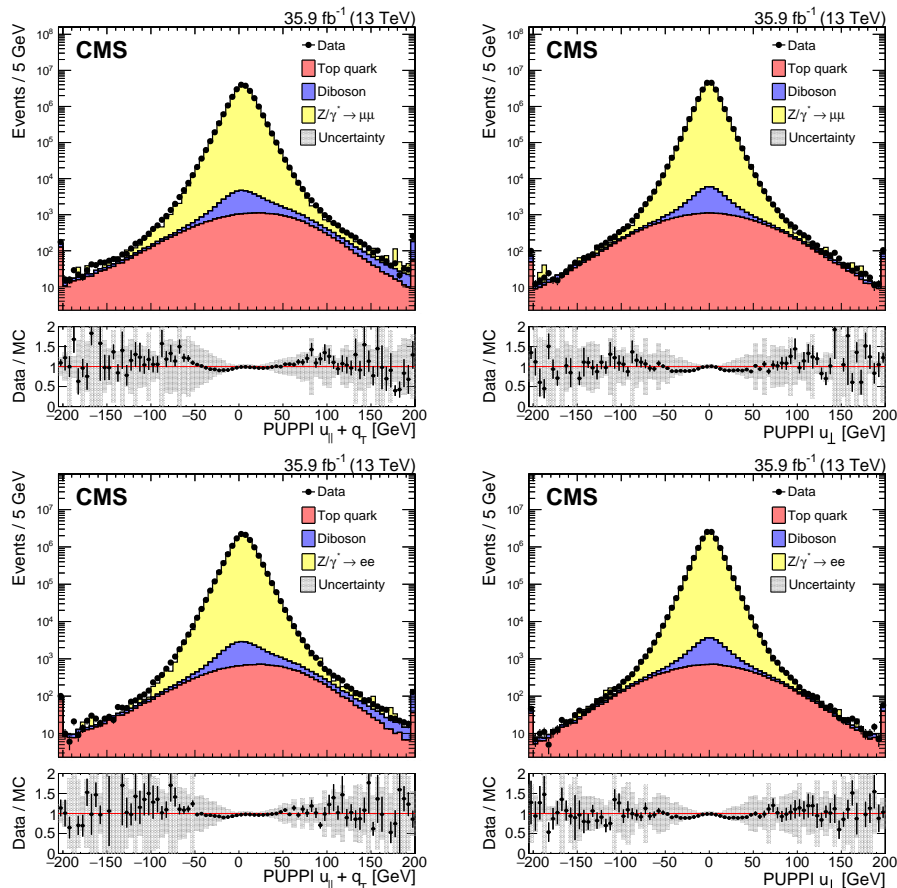
Figure 12. Upper panels: distributions of the $u_\parallel + q_T$ and $u_\perp$ components of the hadronic recoil, in data (filled markers) and simulation (solid histograms), for the $Z \rightarrow \mu^+\mu^-$ (upper) and $Z \rightarrow e^+e^-$ (lower) events. The first and the last bins include all events below -195 and above +195, respectively. Lower panel: data-to-simulation ratio. The band corresponds to the systematic uncertainties due to the JES, the JER, and variations in the E_U added in quadrature, estimated from the $Z \rightarrow e^+e^-$ sample.

Figure 13 shows the PUPPI p_T^{miss} response as a function of q_T for data and simulation in $Z \rightarrow \mu^+\mu^-$ and $Z \rightarrow e^+e^-$ events. The response rises to unity for $Z \rightarrow \mu^+\mu^-$ events at a Z boson p_T of 150 GeV, whereas for PF p_T^{miss} the reaches unity at 100 GeV . The slower rise of the response to unity is due to the removal of PF candidates that are wrongly associated with pileup interactions by the PUPPI algorithm. As in PF p_T^{miss}, there is no response correction for the E_U in the PUPPI p_T^{miss}, which results in an underestimated response at low q_T. The response of p_T^{miss} agrees for the different samples within 2%.

The resolution of the PUPPI p_T^{miss} for the $u_\parallel$ and $u_\perp$ components of the hadronic recoil as a function N_{vtx} is shown in figure 14. To compare the resolution of p_T^{miss} consistently across the
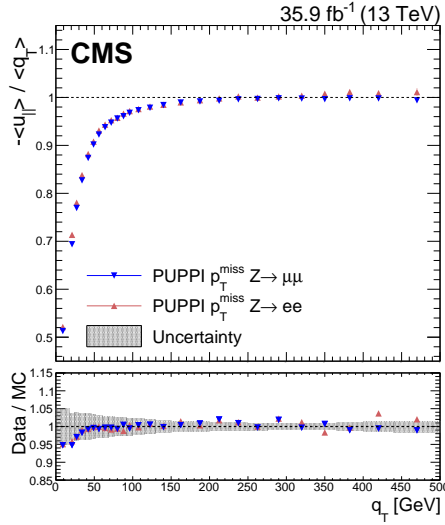
Figure 13. Upper panel: response of PUPPI p_T^{miss}, defined as $-\langle u_\parallel \rangle / \langle q_T \rangle$, in data in $Z \rightarrow \mu^+\mu^-$ and $Z \rightarrow e^+e^-$ events. Lower panel: ratio of the PUPPI p_T^{miss} response in data and simulation. The band corresponds to the systematic uncertainties due to the JES, the JER, and variations in the E_U added in quadrature, estimated from the $Z \rightarrow e^+e^-$ sample.

samples, the resolution in each sample is corrected for the differences observed in the scale. The resolutions measured in different samples are in good agreement. In figure 15, the results obtained for the case of PUPPI p_T^{miss} are overlaid with the ones obtained using PF p_T^{miss}. Compared to the case of PF p_T^{miss}, the resolutions show a much reduced dependence on the number of pileup interactions.

The resolutions in different samples are parametrized using eq. (9.1), and the results of the parameterization are given in table 4. Good agreement is observed between data and simulation and no additional corrections are used in the p_T^{miss} calibration. Each additional pileup interaction degrades the resolution of each component by up to 2 GeV . This degradation in resolution corresponds to half of that observed in the case of PF p_T^{miss}.

Table 4. Parameterization results of the resolution curves for PUPPI $u_\parallel$ and $u_\perp$ components as a function of N_{vtx}. The parameter values for σ_c are obtained from data and simulation, and the values for σ_{PU} are obtained from data, along with the ratio R_{PU} of data and simulation. The uncertainties displayed for both the components are obtained from the fit, and for simulation the JES, the JER, and E_U uncertainties are added in quadrature.

Process	σ_c(data)[GeV]	σ_c(MC)[GeV]	σ_{PU}(data)[GeV]	$R_{PU} = \sigma_{PU}$(data)$/\sigma_{PU}$(MC)
		$u_\parallel$ component		
$Z \rightarrow \mu^+\mu^-$	18.9 ± 0.05	17.5 ± 0.74	1.93 ± 0.02	0.97 ± 0.11
$Z \rightarrow e^+e^-$	18.9 ± 0.06	17.4 ± 0.80	1.94 ± 0.03	0.98 ± 0.12
		$u_\perp$ component		
$Z \rightarrow \mu^+\mu^-$	14.2 ± 0.04	13.6 ± 0.59	1.78 ± 0.01	0.97 ± 0.09
$Z \rightarrow e^+e^-$	14.3 ± 0.05	13.6 ± 0.59	1.80 ± 0.02	0.96 ± 0.09

– 23 –
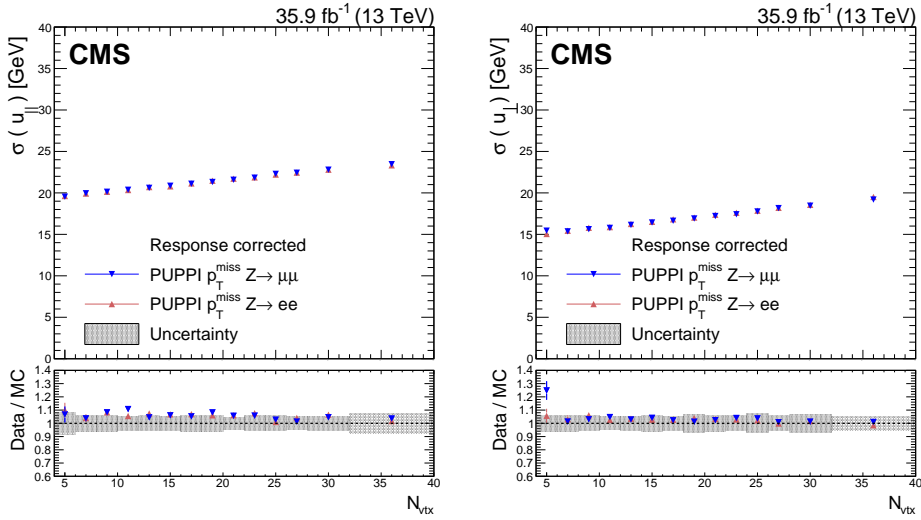
Figure 14. PUPPI p_T^{miss} resolution of the $u_\parallel$ (left) and $u_\perp$ (right) components of the hadronic recoil as a function of N_{vtx}, in $Z \to \mu^+\mu^-$ and $Z \to e^+e^-$ events. In each plot, the upper panel shows the resolution in data, whereas the lower panel shows the ratio of data to simulation. The band corresponds to the systematic uncertainties due to the JES, the JER, and variations in the E_U added in quadrature, estimated from the $Z \to e^+e^-$ sample.
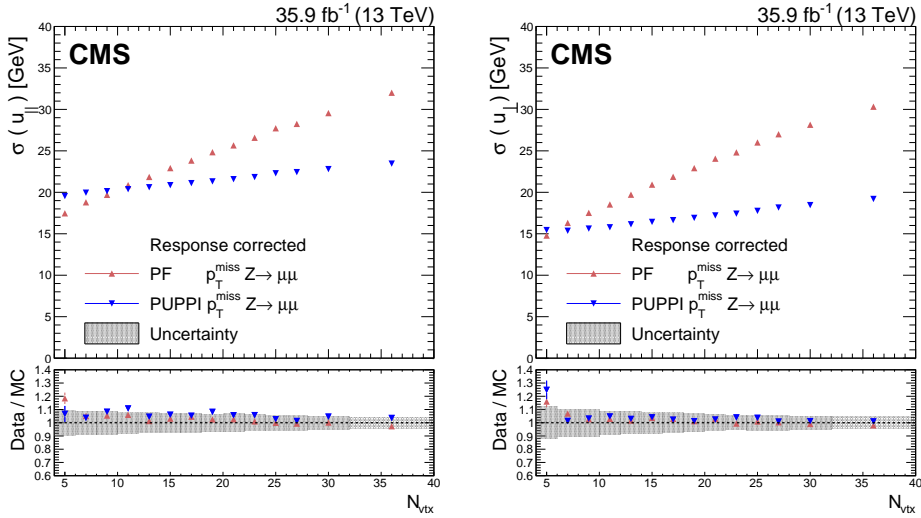
Figure 15. Upper panels: PUPPI and PF p_T^{miss} resolution of $u_\parallel$ (left) and $u_\perp$ (right) components of the hadronic recoil as a function of N_{vtx}, in $Z \to \mu^+\mu^-$ events. Lower panels: data-to-simulation ratio. The systematic uncertainties due to the JES, the JER, and variations in the E_U are added in quadrature and represented by the shaded band.

9.3 Performance of p_T^{miss} in single-lepton samples

Also single-lepton events, which contain genuine p_T^{miss}, are utilized to study the performance of the p_T^{miss} algorithms. In events with a W boson, the magnitude of the p_T^{miss} is approximately equal to the p_T of the lepton, and its resolution is dominated by the hadronic recoil.

In figure 16, the PF and PUPPI p_T^{miss} distributions are compared in single-muon and -electron samples, where the normalization of the QCD multijet background is corrected using the method discussed in section 6.4. A larger discrimination between events with and without genuine p_T^{miss} is observed for the PUPPI p_T^{miss} algorithm.
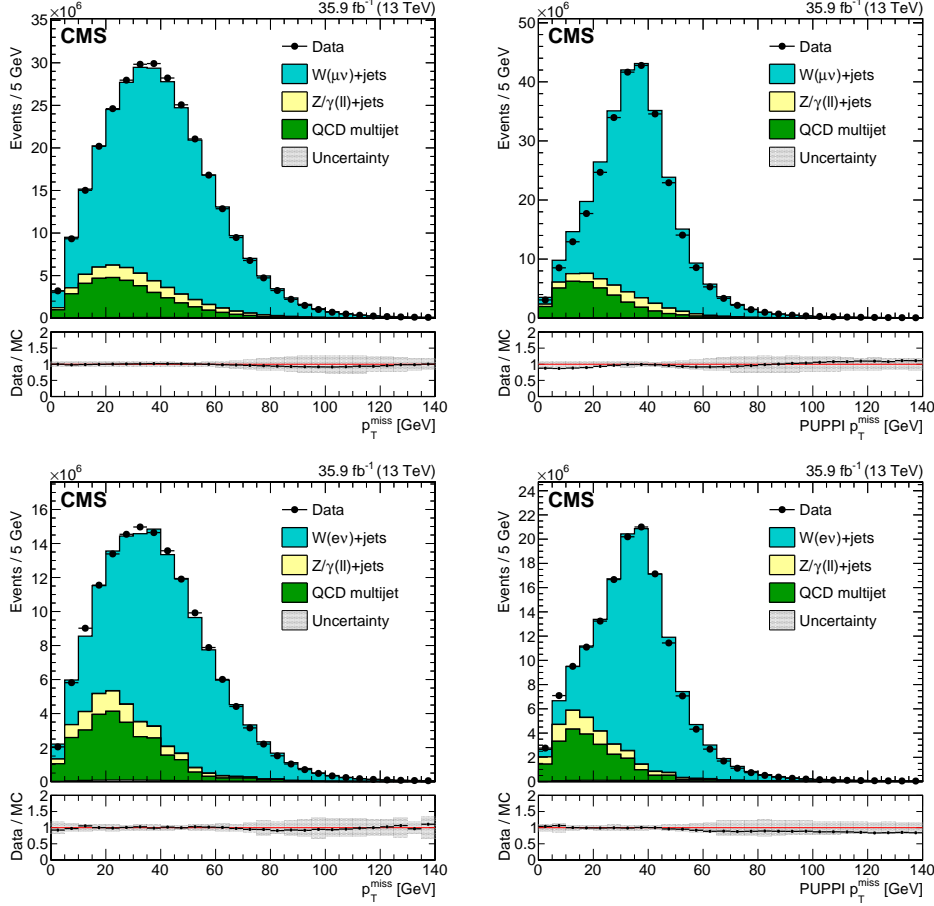
Figure 16. The PF (left) and PUPPI (right) p_T^{miss} distributions are shown for single-muon (upper) and single-electron (lower) events. The last bin includes all events with $p_T^{miss} > 135$ GeV. In all the distributions, the lower panel shows the ratio of data to simulation. The systematic uncertainties due to the JES, the JER, and variations in the E_U are added in quadrature and represented by the shaded band.

The transverse mass (M_T) of the lepton-$\vec{p}_T^{miss}$ system is compared between the algorithms, as shown in figure 17. The M_T of the system is computed as:

$$M_T = \sqrt{2 p_T^{miss} p_T^{lepton} (1 - \cos \Delta\phi)}, \tag{9.3}$$

where p_T^{lepton} is the p_T of the lepton, and $\Delta\phi$ is the angle between $\vec{p}_T^{lepton}$ and $\vec{p}_T^{miss}$. As in the p_T^{miss} case, the PUPPI algorithm has a better discrimination between events with and without genuine p_T^{miss}. In addition, the spread of the Jacobian mass peak is smaller when M_T is computed using PUPPI p_T^{miss}. The summary of the mean and the spread of the Jacobian mass peak, calculated in simulated W+jets events, is provided in table 5. Utilizing PUPPI p_T^{miss} for the M_T calculation results in a 10–15% relative improvement in the resolution of the Jacobian mass peak with respect to PF p_T^{miss}.
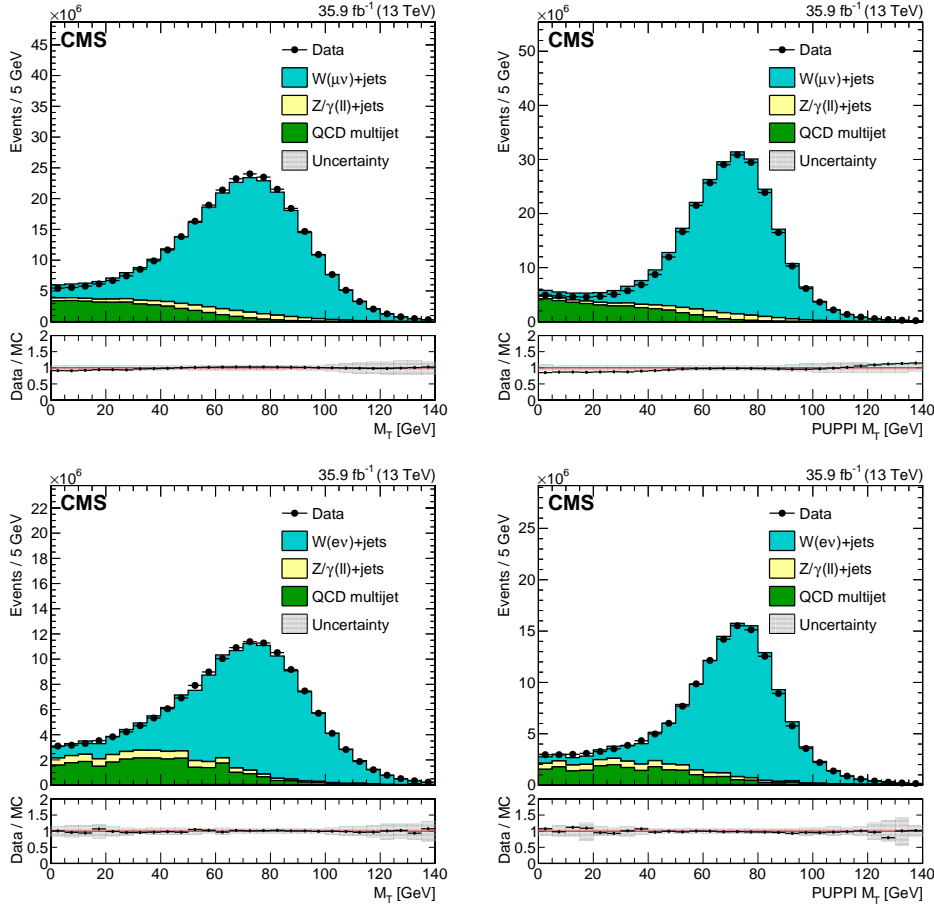
Figure 17. The PF (left) and PUPPI (right) M_T distribution are shown for single-muon (upper) and single-electron (lower) events. The last bin includes all events with $M_T > 135$ GeV In all the distributions, the lower panel shows the ratio of data to simulation. The systematic uncertainties due to the JES, the JER, and variations in the E_U are added in quadrature and represented by the shaded band.

10   The p_T^{miss} significance

The ability to distinguish between events with genuine p_T^{miss} and those with spurious p_T^{miss} is important for analyses targeting signatures with weakly interacting particles. The p_T^{miss} significance variable, denoted by $\mathcal{S}$, quantifies the degree of compatibility of p_T^{miss} with zero on an event-by-event basis, and it is computed using all clustered objects and the E_U in each event. A factorized approach leads to the construction of a significance variable that is applicable to a variety of event topologies. The variable is described in detail in refs. [13, 14]. Here we give an overview of updates and performance studies conducted using the 13 TeV data set.

The significance is defined as the log-likelihood ratio

$$\mathcal{S} \equiv 2\ln\left(\frac{\mathcal{L}(\vec{\varepsilon} = \sum \vec{\varepsilon}_i)}{\mathcal{L}(\vec{\varepsilon} = 0)}\right), \tag{10.1}$$

where the $\vec{\varepsilon}$ is the true p_T^{miss} and $\sum \vec{\varepsilon}_i$ is the observed p_T^{miss}. In the numerator, we evaluate the likelihood that the true value of p_T^{miss} equals the observed value, while the denominator corresponds

Table 5. The summary of the mean and the spread of the Jacobian mass peak in the M_T distribution in single-lepton events for PF and PUPPI p_T^{miss} algorithms. The results are obtained using simulated W+jets events.

Process	Mean [GeV]	RMS [GeV]	Mean [GeV]	RMS [GeV]
	PF algorithm		PUPPI algorithm	
	$0 < N_{vtx} \leq 20$			
$W \to \mu\nu$	76.26 ± 0.01	15.01 ± 0.01	73.44 ± 0.01	13.01 ± 0.01
$W \to e\nu$	77.46 ± 0.01	15.37 ± 0.01	74.61 ± 0.01	13.18 ± 0.01
	$20 < N_{vtx} \leq 30$			
$W \to \mu\nu$	78.58 ± 0.01	16.45 ± 0.01	74.21 ± 0.01	13.65 ± 0.01
$W \to e\nu$	79.96 ± 0.01	16.74 ± 0.01	75.45 ± 0.01	13.87 ± 0.01
	$N_{vtx} \geq 30$			
$W \to \mu\nu$	80.75 ± 0.02	17.47 ± 0.01	75.29 ± 0.01	14.43 ± 0.01
$W \to e\nu$	82.26 ± 0.03	17.73 ± 0.02	76.68 ± 0.02	14.70 ± 0.02

to the null hypothesis, i.e., that the true p_T^{miss} is zero. To a very good approximation the likelihood $\mathcal{L}(\vec{\varepsilon})$ has the form of a Gaussian distribution. The significance can be therefore written as:

$$\mathcal{S} = \left(\sum \vec{\varepsilon}_i \right)^T \mathbf{V}^{-1} \left(\sum \vec{\varepsilon}_i \right), \tag{10.2}$$

where $\mathbf{V}$ is the 2×2 p_T^{miss} covariance matrix. In this formulation, $\mathcal{S}$ is conveniently a χ^2 variable with two degrees of freedom (one degree of freedom each for the x– and y-axis components of p_T^{miss}) for events with zero true p_T^{miss}.

The covariance matrix $\mathbf{V}$ in eq. (10.2) models the p_T^{miss} resolution in each event. It is constructed by propagating the individual resolutions of the objects entering the p_T^{miss} sum. In most cases, the p_T^{miss} resolution captured in $\mathbf{V}$ is primarily determined by the hadronic components of the event, which includes jets with $p_T > 15\,\text{GeV}$ and the E_U. Jets enter the total covariance $\mathbf{V}$ with an individual covariance of the form:

$$\mathbf{U} = \begin{pmatrix} \sigma_{p_T}^2 & 0 \\ 0 & p_T^2 \sigma_\phi^2 \end{pmatrix}, \tag{10.3}$$

where the quantities σ_{p_T} and σ_ϕ are measured and then recalculated based on a combination of simulation and data control samples, as explained in ref. [14]. The momenta of the PF candidates i that is not included in a jet are summed vectorially, and the resulting momentum is assigned to a single pseudo-object i.e., $\vec{p}_T = \sum_i \vec{p}_{Ti}$. The resolution of this pseudo-object is parameterized by the scalar p_T sum of its constituents:

$$\sigma_{uc}^2 = \sigma_0^2 + \sigma_s^2 \sum_{i=1}^n |\vec{p}_{Ti}|, \tag{10.4}$$

where the values of σ_0^2 and σ_s^2 are determined using control samples in data, as explained in ref. [14]. The resolution of this object is assumed to be isotropic in the transverse plane of the detector. The finite (small) resolution of electrons and muons is negligible, compared to the hadronic component of the event, and hence their contribution to $\mathbf{V}$ is neglected

10.1 Unclustered energy studies

The unclustered PF candidates are combined into a pseudo-object. Its resolution should be isotropic in the transverse plane, and proportional to the magnitude of the p_T of the pseudo-object. This approach, called the "standard" method of $\mathcal{S}$ in what follows, is motivated by its simplicity, and shows good agreement between data and simulation. The diagonal elements of the contribution of the E_U to the covariance matrix are given by eq. (10.4).

During the data-taking run, an alternative method to obtain the covariance matrix was explored, the so-called "jackknife technique" [32, 33]. The jackknife technique allows the estimation of a covariance matrix that is not necessarily isotropic, and also includes offdiagonal elements. The covariance matrix is calculated using the "delete-1 method", in which a single PF candidate is removed. This approach leads to $N - 1$ samples per event, with N the total numbers of constituents contributing to the E_U. The covariance matrix takes the form:

$$\hat{V}_{ij} = \frac{N-1}{N} \sum_{k=1}^{N} (p_i^k - \overline{p}_i)(p_j^k - \overline{p}_j),$$

(10.5)

where k is the removed candidate, p_i^k and p_j^k are x and y components of the E_U calculated after removing the k-th candidate, whereas the indexes i and j both span x and y. The $\overline{p}_i$ and $\overline{p}_j$ are mean values of x and y components of the E_U over all samples, defined as:

$$\overline{p}_{i,j} = \frac{1}{N} \sum_{k=1}^{N} p_{i,j}^k.$$

(10.6)

Again, the resolution is scaled by the parameters tuned in data and simulated samples, referred to as a_x and a_y. The parameters are determined following a similar approach as in the standard method of $\mathcal{S}$. The resolutions of the components of the E_U are then defined as

$$\begin{aligned}
\sigma_x^2 &= a_x^2 \, \hat{V}_{xx}, \\
\sigma_{xy}^2 &= a_x \, a_y \, \hat{V}_{xy}, \\
\sigma_y^2 &= a_y^2 \, \hat{V}_{yy}.
\end{aligned}$$

(10.7)

10.2 Performance evaluation

The discrimination power between events with genuine p_T^{miss} (signal) and those without (background), of the two versions of $\mathcal{S}$, the standard and the jackknife, and the p_T^{miss} algorithms, is compared in terms of receiver operating characteristic (ROC) curves. The results are shown in figure 18 using simulated dimuon events (a sample dominated by events with no genuine p_T^{miss}) and single-electron events (a sample dominated by events with genuine p_T^{miss}). No significant difference between the two $\mathcal{S}$ versions is observed. Both versions of $\mathcal{S}$ offer better signal-to-background separation than p_T^{miss}. For example, choosing a working point with 1% background efficiency the $\mathcal{S}$ variables offer 5% higher signal efficiency than p_T^{miss}. For the remainder of the section, we focus only on the standard version of $\mathcal{S}$.

The performance of $\mathcal{S}$ is evaluated in data using dilepton and single-lepton events. The results are displayed in figures 19 and 20, respectively, for different jet multiplicities. In figure 19, where
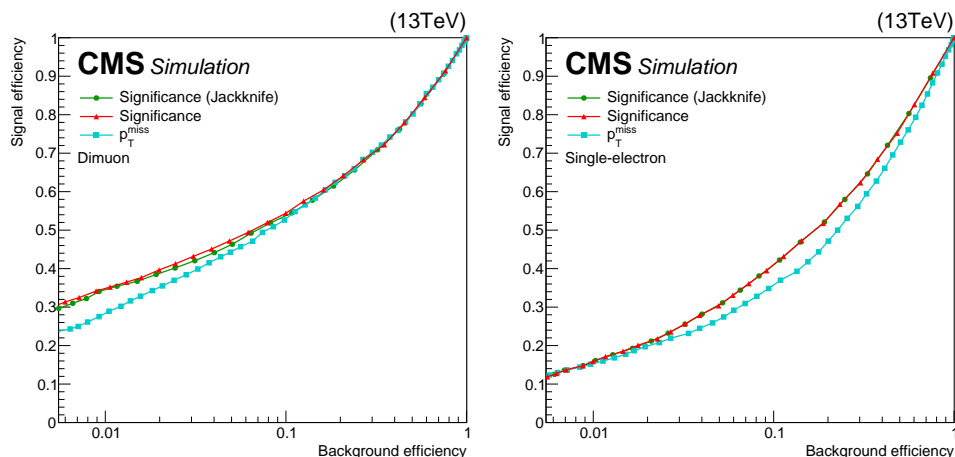
Figure 18. ROC curves comparing the signal (events with genuine p_T^{miss}) versus background (events with no genuine p_T^{miss}) efficiency for the standard version of $\mathcal{S}$ (red line), the jackknife version of $\mathcal{S}$ (yellow line), and p_T^{miss} (cyan line) using simulated dimuon events (left) and single-electron events (right). Similar performance is observed between the two versions of $\mathcal{S}$, which perform better than p_T^{miss} especially in regions with small background efficiency.

events with no genuine p_T^{miss} dominate, the core of the $\mathcal{S}$ spectrum follows an ideal χ^2 distribution. For large values of $\mathcal{S}$ the spectrum begins to deviate from a perfect χ^2 distribution as the processes with genuine p_T^{miss} become important. This deviation also has contributions from the nonGaussian tails of the jet p_T resolution function, which are not considered in eq. (10.2). A detailed discussion of the treatment of nonGaussian resolutions can be found in [14].

The stability of $\mathcal{S}$ against pileup is studied using dimuon and single-electron events. Figure 21 displays the average $\mathcal{S}$ as a function of N_{vtx}. In the dimuon sample, dominated by events with no genuine p_T^{miss}, the value of $\mathcal{S}$ is robust against pileup, with an average value of ~ 2, as expected for a χ^2 variable with two degrees of freedom. This behavior can be explained qualitatively with the following arguments. In the case of events with no genuine p_T^{miss}, the contribution of pileup affects in a similar manner both p_T^{miss} and the variance of p_T^{miss}, since both are dominated by the hadronic resolution. This results in an essentially constant value of $\mathcal{S}$ which does not depend on the number of pileup interactions. However, in events with genuine p_T^{miss}, as in the single-electron sample, pileup has a small impact on p_T^{miss}, whereas the impact on the resolution in p_T^{miss} is similar to the case of no genuine p_T^{miss}, leading to a decrease of $\mathcal{S}$ as pileup increases. This results in a degradation in the performance of $\mathcal{S}$ when N_{vtx} is large.

11   Summary

The performance of missing transverse momentum (p_T^{miss}) reconstruction algorithms in events with or without genuine p_T^{miss} is presented. The results are based on a sample of proton-proton collisions recorded by the CMS experiment at $\sqrt{s} = 13$ TeV in 2016, corresponding to an integrated luminosity of 35.9 fb^{-1}.

The performance of algorithms used to identify and remove events with anomalous p_T^{miss} is also studied in events with one or more jets. The scale and resolution of p_T^{miss} is determined using
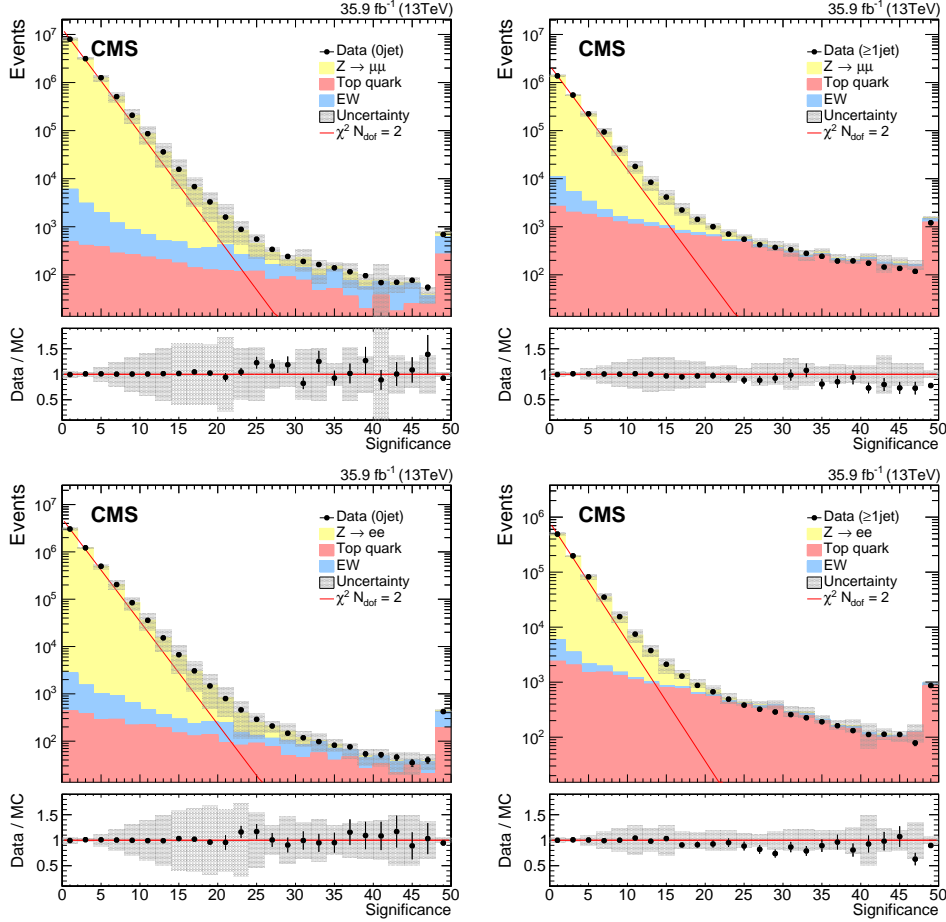
Figure 19. Distributions of $\mathcal{S}$ in data and simulation in dimuon (upper) and dielectron (lower) samples, for events with zero jet (left) and ≥ 1 jet (right). The last bin includes all events with $\mathcal{S} > 48$. The red straight line corresponds to a χ^2 distribution with two degrees of freedom. The bands in the bottom panel display systematic uncertainties due to effects from the JES, the JER, and variations in the E_U in simulation. Good agreement between data and simulation is observed.

events with an identified leptonically decaying Z boson or an isolated photon. The measured scale and resolution in data are in agreement with the expectations from simulation. Also presented is the performance of an advanced p_T^{miss} reconstruction algorithm, the "pileup per particle identification" p_T^{miss}, specifically developed to cope with the large pileup collisions expected at the high-luminosity LHC. This algorithm shows a significantly reduced dependence of the p_T^{miss} resolution on the number of pileup collisions ($\gtrsim 10$), particularly important for the upcoming LHC data-taking periods. Finally, the performance of an algorithm ($\mathcal{S}$) used to estimate the compatibility of the reconstructed p_T^{miss} with the hypothesis that it originates from resolution effects, was studied. The $\mathcal{S}$ shows improved performance in discriminating between events with and without genuine p_T^{miss} compared to the traditional p_T^{miss} reconstruction algorithms.
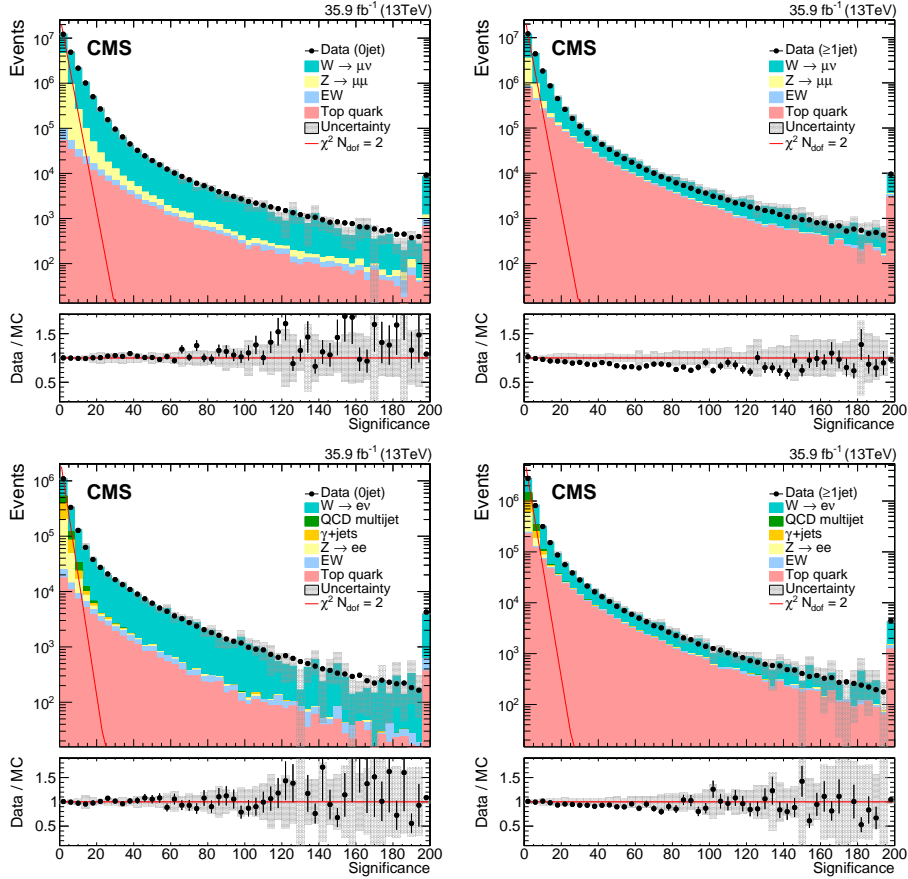
Figure 20. Distributions of $\mathcal{S}$ in data and simulation in single-muon (upper) and single-electron (lower) samples, for events with zero jet (left) and ≥ 1 jet (right). The last bin includes all events with $\mathcal{S} > 48$. The red straight line corresponds to a χ^2 distribution with two degrees of freedom. The bands in the bottom panel display systematic uncertainties due to effects from the JES, the JER, and variations in the E_U in simulation. Good agreement between data and simulation is observed.
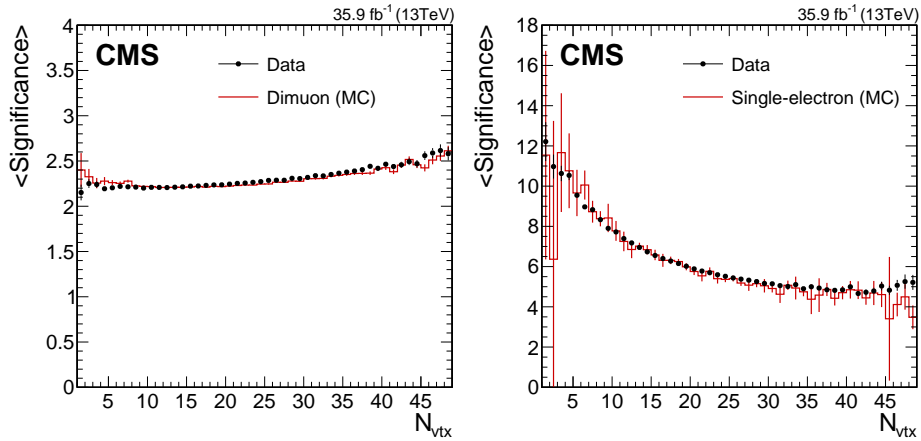
Figure 21. Dependence of the average $\mathcal{S}$ on pileup, for dimuon (left) and single-electron (right) events. Weak dependence is observed for processes with no genuine p_T^{miss}, whereas in events with genuine p_T^{miss} the behavior of $\mathcal{S}$ depends strongly on primary vertex multiplicity.

Acknowledgments

References

[1] CMS collaboration, *The CMS Experiment at the CERN LHC*, 2008 *JINST* **3** S08004.

[2] L. Evans and P. Bryant, *LHC Machine*, 2008 *JINST* **3** S08001.

[3] CMS collaboration, *Description and performance of track and primary-vertex reconstruction with the CMS tracker*, 2014 *JINST* **9** P10009 [arXiv:1405.6569].

[4] CMS collaboration, *Performance of the CMS muon detector and muon reconstruction with proton-proton collisions at $\sqrt{s}$ = 13 TeV*, 2018 *JINST* **13** P06015 [arXiv:1804.04528].

[5] CMS collaboration, *The CMS trigger system*, 2017 *JINST* **12** P01020 [arXiv:1609.02366].

[6] CMS collaboration, *Particle-flow reconstruction and global event description with the CMS detector*, 2017 *JINST* **12** P10003 [arXiv:1706.04965].

[7] CMS collaboration, *Performance of Photon Reconstruction and Identification with the CMS Detector in Proton-Proton Collisions at $\sqrt{s}$ = 8 TeV*, 2015 *JINST* **10** P08010 [arXiv:1502.02702].

[8] CMS collaboration, *Performance of Electron Reconstruction and Selection with the CMS Detector in Proton-Proton Collisions at $\sqrt{s}$ = 8 TeV*, 2015 *JINST* **10** P06005 [arXiv:1502.02701].

[9] CMS collaboration, *Reconstruction and identification of τ lepton decays to hadrons and ν_τ at CMS*, 2016 *JINST* **11** P01019 [arXiv:1510.07488].

[10] M. Cacciari, G.P. Salam and G. Soyez, *The anti-k_T jet clustering algorithm*, *JHEP* **04** (2008) 063 [arXiv:0802.1189].

[11] CMS collaboration, *Jet energy scale and resolution in the CMS experiment in pp collisions at 8 TeV*, 2017 *JINST* **12** P02014 [arXiv:1607.03663].

[12] CMS collaboration, *Identification of heavy-flavour jets with the CMS detector in pp collisions at 13 TeV*, 2018 *JINST* **13** P05011 [arXiv:1712.07158].

[13] CMS collaboration, *Missing transverse energy performance of the CMS detector*, 2011 *JINST* **6** P09001 [arXiv:1106.5048].

[14] CMS collaboration, *Performance of the CMS missing transverse momentum reconstruction in pp data at $\sqrt{s} = 8$ TeV*, 2015 *JINST* **10** P02006 [arXiv:1411.0511].

[15] D. Bertolini, P. Harris, M. Low and N. Tran, *Pileup Per Particle Identification*, *JHEP* **10** (2014) 059 [arXiv:1407.6013].

[16] CMS collaboration, *Jet algorithms performance in 13 TeV data*, CMS Physics Analysis Summary, CMS-PAS-JME-16-003 (2017).

[17] J. Alwall, R. Frederix, S. Frixione, V. Hirschi, F. Maltoni, O. Mattelaer et al., *The automated computation of tree-level and next-to-leading order differential cross sections and their matching to parton shower simulations*, *JHEP* **07** (2014) 079 [arXiv:1405.0301].

[18] C. Oleari, *The POWHEG-BOX*, *Nucl. Phys. Proc. Suppl.* **205-206** (2010) 36 [arXiv:1007.3893].

[19] S. Alioli, P. Nason, C. Oleari and E. Re, *NLO single-top production matched with shower in POWHEG: s- and t-channel contributions*, *JHEP* **09** (2009) 111 [*Erratum ibid.* **1002** (2010) 011] [arXiv:0907.4076].

[20] T. Sjöstrand, S. Ask, J.R. Christiansen, R. Corke, N. Desai, P. Ilten et al., *An Introduction to PYTHIA 8.2*, *Comput. Phys. Commun.* **191** (2015) 159 [arXiv:1410.3012].

[21] CMS collaboration, *Event generator tunes obtained from underlying event and multiparton scattering measurements*, *Eur. Phys. J.* **C 76** (2016) 155 [arXiv:1512.00815].

[22] M.L. Mangano, M. Moretti, F. Piccinini and M. Treccani, *Matching matrix elements and shower evolution for top-quark production in hadronic collisions*, *JHEP* **01** (2007) 013 [hep-ph/0611129].

[23] R. Frederix and S. Frixione, *Merging meets matching in MC@NLO*, *JHEP* **12** (2012) 061 [arXiv:1209.6215].

[24] NNPDF collaboration, *Parton distributions for the LHC Run II*, *JHEP* **04** (2015) 040 [arXiv:1410.8849].

[25] GEANT4 collaboration, *GEANT4: A Simulation toolkit*, *Nucl. Instrum. Meth.* **A 506** (2003) 250.

[26] CMS collaboration, *CMS Luminosity Measurements for the 2016 Data Taking Period*, CMS Physics Analysis Summary, CMS-PAS-LUM-17-001 (2017).

[27] Particle Data Group collaboration, *Review of Particle Physics*, *Phys. Rev.* **D 98** (2018) 030001.

[28] CMS collaboration, *Technical proposal for the upgrade of the CMS detector through 2020*, CERN-LHCC-2011-006, LHCC-P-004 (2011).

[29] CMS collaboration, *Identification and Filtering of Uncharacteristic Noise in the CMS Hadron Calorimeter*, 2010 *JINST* **5** T03014 [arXiv:0911.4881].

[30] N. Tosi, *The CMS beam halo monitor at the LHC: implementation and first measurements*, in *Proceedings, 5th International Beam Instrumentation Conference (IBIC 2016)*, Barcelona, Spain, 11–15 September 2016, paper TUPG20.

[31] CMS collaboration, *2017 tracking performance plots*, CMS Detector Performance Report, CMS-DP-2017-015 (2017).

[32] M.H. Quenouille, *Approximate tests of correlation in time-series*, *J. Roy. Stat. Soc.* **B 11** (1949) 68.

[33] J.W. Tukey, *Bias and confidence in not quite large samples*, *Ann. Math. Statist.* **29** (1958) 1261.

The CMS collaboration

Yerevan Physics Institute, Yerevan, Armenia

A.M. Sirunyan, A. Tumasyan

Institut für Hochenergiephysik, Wien, Austria

W. Adam, F. Ambrogi, E. Asilar, T. Bergauer, J. Brandstetter, M. Dragicevic, J. Erö, A. Escalante Del Valle, M. Flechl, R. Frühwirth[1], V.M. Ghete, J. Hrubec, M. Jeitler[1], N. Krammer, I. Krätschmer, D. Liko, T. Madlener, I. Mikulec, N. Rad, H. Rohringer, J. Schieck[1], R. Schöfbeck, M. Spanring, D. Spitzbart, A. Taurok, W. Waltenberger, J. Wittmann, C.-E. Wulz[1], M. Zarucki

Institute for Nuclear Problems, Minsk, Belarus

V. Chekhovsky, V. Mossolov, J. Suarez Gonzalez

Universiteit Antwerpen, Antwerpen, Belgium

E.A. De Wolf, D. Di Croce, X. Janssen, J. Lauwers, M. Pieters, H. Van Haevermaet, P. Van Mechelen, N. Van Remortel

Vrije Universiteit Brussel, Brussel, Belgium

S. Abu Zeid, F. Blekman, J. D'Hondt, J. De Clercq, K. Deroover, G. Flouris, D. Lontkovskyi, S. Lowette, I. Marchesini, S. Moortgat, L. Moreels, Q. Python, K. Skovpen, S. Tavernier, W. Van Doninck, P. Van Mulders, I. Van Parijs

Université Libre de Bruxelles, Bruxelles, Belgium

D. Beghin, B. Bilin, H. Brun, B. Clerbaux, G. De Lentdecker, H. Delannoy, B. Dorney, G. Fasanella, L. Favart, R. Goldouzian, A. Grebenyuk, A.K. Kalsi, T. Lenzi, J. Luetic, N. Postiau, E. Starling, L. Thomas, C. Vander Velde, P. Vanlaer, D. Vannerom, Q. Wang

Ghent University, Ghent, Belgium

T. Cornelis, D. Dobur, A. Fagot, M. Gul, I. Khvastunov[2], D. Poyraz, C. Roskas, D. Trocino, M. Tytgat, W. Verbeke, B. Vermassen, M. Vit, N. Zaganidis

Université Catholique de Louvain, Louvain-la-Neuve, Belgium

H. Bakhshiansohi, O. Bondu, S. Brochet, G. Bruno, C. Caputo, P. David, C. Delaere, M. Delcourt, A. Giammanco, G. Krintiras, V. Lemaitre, A. Magitteri, K. Piotrzkowski, A. Saggio, M. Vidal Marono, P. Vischia, S. Wertz, J. Zobec

Centro Brasileiro de Pesquisas Fisicas, Rio de Janeiro, Brazil

F.L. Alves, G.A. Alves, M. Correa Martins Junior, G. Correia Silva, C. Hensel, A. Moraes, M.E. Pol, P. Rebello Teles

Universidade do Estado do Rio de Janeiro, Rio de Janeiro, Brazil

E. Belchior Batista Das Chagas, W. Carvalho, J. Chinellato[3], E. Coelho, E.M. Da Costa, G.G. Da Silveira[4], D. De Jesus Damiao, C. De Oliveira Martins, S. Fonseca De Souza, H. Malbouisson, D. Matos Figueiredo, M. Melo De Almeida, C. Mora Herrera, L. Mundim, H. Nogima, W.L. Prado Da Silva, L.J. Sanchez Rosas, A. Santoro, A. Sznajder, M. Thiel, E.J. Tonelli Manganote[3], F. Torres Da Silva De Araujo, A. Vilela Pereira

Universidade Estadual Paulista ^{a}, Universidade Federal do ABC ^{b}, São Paulo, Brazil

S. Ahuja^a, C.A. Bernardes^a, L. Calligaris^a, T.R. Fernandez Perez Tomei^a, E.M. Gregores^b, P.G. Mercadante^b, S.F. Novaes^a, SandraS. Padula^a

Institute for Nuclear Research and Nuclear Energy, Bulgarian Academy of Sciences, Sofia, Bulgaria

A. Aleksandrov, R. Hadjiiska, P. Iaydjiev, A. Marinov, M. Misheva, M. Rodozov, M. Shopova, G. Sultanov

University of Sofia, Sofia, Bulgaria

A. Dimitrov, L. Litov, B. Pavlov, P. Petkov

Beihang University, Beijing, China

W. Fang[5], X. Gao[5], L. Yuan

Institute of High Energy Physics, Beijing, China

M. Ahmad, J.G. Bian, G.M. Chen, H.S. Chen, M. Chen, Y. Chen, C.H. Jiang, D. Leggat, H. Liao, Z. Liu, S.M. Shaheen[6], A. Spiezia, J. Tao, Z. Wang, E. Yazgan, H. Zhang, S. Zhang[6], J. Zhao

State Key Laboratory of Nuclear Physics and Technology, Peking University, Beijing, China

Y. Ban, G. Chen, A. Levin, J. Li, L. Li, Q. Li, Y. Mao, S.J. Qian, D. Wang

Tsinghua University, Beijing, China

Y. Wang

Universidad de Los Andes, Bogota, Colombia

C. Avila, A. Cabrera, C.A. Carrillo Montoya, L.F. Chaparro Sierra, C. Florez, C.F. González Hernández, M.A. Segura Delgado

University of Split, Faculty of Electrical Engineering, Mechanical Engineering and Naval Architecture, Split, Croatia

B. Courbon, N. Godinovic, D. Lelas, I. Puljak, T. Sculac

University of Split, Faculty of Science, Split, Croatia

Z. Antunovic, M. Kovac

Institute Rudjer Boskovic, Zagreb, Croatia

V. Brigljevic, D. Ferencek, K. Kadija, B. Mesic, A. Starodumov[7], T. Susa

University of Cyprus, Nicosia, Cyprus

M.W. Ather, A. Attikis, M. Kolosova, G. Mavromanolakis, J. Mousa, C. Nicolaou, F. Ptochos, P.A. Razis, H. Rykaczewski

Charles University, Prague, Czech Republic

M. Finger[8], M. Finger Jr.[8]

Escuela Politecnica Nacional, Quito, Ecuador

E. Ayala

Universidad San Francisco de Quito, Quito, Ecuador

E. Carrera Jarrin

Academy of Scientific Research and Technology of the Arab Republic of Egypt, Egyptian Network of High Energy Physics, Cairo, Egypt

M.A. Mahmoud[9,10], A. Mahrous[11], E. Salama[10,12]

National Institute of Chemical Physics and Biophysics, Tallinn, Estonia

S. Bhowmik, A. Carvalho Antunes De Oliveira, R.K. Dewanjee, K. Ehataht, M. Kadastik, M. Raidal, C. Veelken

Department of Physics, University of Helsinki, Helsinki, Finland

P. Eerola, H. Kirschenmann, J. Pekkanen, M. Voutilainen

Helsinki Institute of Physics, Helsinki, Finland

J. Havukainen, J.K. Heikkilä, T. Järvinen, V. Karimäki, R. Kinnunen, T. Lampén, K. Lassila-Perini, S. Laurila, S. Lehti, T. Lindén, P. Luukka, T. Mäenpää, H. Siikonen, E. Tuominen, J. Tuominiemi

Lappeenranta University of Technology, Lappeenranta, Finland

T. Tuuva

IRFU, CEA, Université Paris-Saclay, Gif-sur-Yvette, France

M. Besancon, F. Couderc, M. Dejardin, D. Denegri, J.L. Faure, F. Ferri, S. Ganjour, A. Givernaud, P. Gras, G. Hamel de Monchenault, P. Jarry, C. Leloup, E. Locci, J. Malcles, G. Negro, J. Rander, A. Rosowsky, M.Ö. Sahin, M. Titov

Laboratoire Leprince-Ringuet, Ecole polytechnique, CNRS/IN2P3, Université Paris-Saclay, Palaiseau, France

A. Abdulsalam[13], C. Amendola, I. Antropov, F. Beaudette, P. Busson, C. Charlot, R. Granier de Cassagnac, I. Kucher, A. Lobanov, J. Martin Blanco, C. Martin Perez, M. Nguyen, C. Ochando, G. Ortona, P. Paganini, P. Pigard, J. Rembser, R. Salerno, J.B. Sauvan, Y. Sirois, A.G. Stahl Leiton, A. Zabi, A. Zghiche

Université de Strasbourg, CNRS, IPHC UMR 7178, Strasbourg, France

J.-L. Agram[14], J. Andrea, D. Bloch, J.-M. Brom, E.C. Chabert, V. Cherepanov, C. Collard, E. Conte[14], J.-C. Fontaine[14], D. Gelé, U. Goerlach, M. Jansová, A.-C. Le Bihan, N. Tonon, P. Van Hove

Centre de Calcul de l'Institut National de Physique Nucleaire et de Physique des Particules, CNRS/IN2P3, Villeurbanne, France

S. Gadrat

Université de Lyon, Université Claude Bernard Lyon 1, CNRS-IN2P3, Institut de Physique Nucléaire de Lyon, Villeurbanne, France

S. Beauceron, C. Bernet, G. Boudoul, N. Chanon, R. Chierici, D. Contardo, P. Depasse, H. El Mamouni, J. Fay, L. Finco, S. Gascon, M. Gouzevitch, G. Grenier, B. Ille, F. Lagarde, I.B. Laktineh, H. Lattaud, M. Lethuillier, L. Mirabito, S. Perries, A. Popov[15], V. Sordini, G. Touquet, M. Vander Donckt, S. Viret

Georgian Technical University, Tbilisi, Georgia

T. Toriashvili[16]

Tbilisi State University, Tbilisi, Georgia

Z. Tsamalaidze[8]

RWTH Aachen University, I. Physikalisches Institut, Aachen, Germany

C. Autermann, L. Feld, M.K. Kiesel, K. Klein, M. Lipinski, M. Preuten, M.P. Rauch, C. Schomakers, J. Schulz, M. Teroerde, B. Wittmer

RWTH Aachen University, III. Physikalisches Institut A, Aachen, Germany

A. Albert, D. Duchardt, M. Erdmann, S. Erdweg, T. Esch, R. Fischer, S. Ghosh, A. Güth, T. Hebbeker, C. Heidemann, K. Hoepfner, H. Keller, L. Mastrolorenzo, M. Merschmeyer, A. Meyer, P. Millet, S. Mukherjee, T. Pook, M. Radziej, H. Reithler, M. Rieger, A. Schmidt, D. Teyssier, S. Thüer

RWTH Aachen University, III. Physikalisches Institut B, Aachen, Germany

G. Flügge, O. Hlushchenko, T. Kress, T. Müller, A. Nehrkorn, A. Nowack, C. Pistone, O. Pooth, D. Roy, H. Sert, A. Stahl[17]

Deutsches Elektronen-Synchrotron, Hamburg, Germany

M. Aldaya Martin, T. Arndt, C. Asawatangtrakuldee, I. Babounikau, K. Beernaert, O. Behnke, U. Behrens, A. Bermúdez Martínez, D. Bertsche, A.A. Bin Anuar, K. Borras[18], V. Botta, A. Campbell, P. Connor, C. Contreras-Campana, V. Danilov, A. De Wit, M.M. Defranchis, C. Diez Pardos, D. Domínguez Damiani, G. Eckerlin, T. Eichhorn, A. Elwood, E. Eren, E. Gallo[19], A. Geiser, J.M. Grados Luyando, A. Grohsjean, M. Guthoff, M. Haranko, A. Harb, H. Jung, M. Kasemann, J. Keaveney, C. Kleinwort, J. Knolle, D. Krücker, W. Lange, A. Lelek, T. Lenz, J. Leonard, K. Lipka, W. Lohmann[20], R. Mankel, I.-A. Melzer-Pellmann, A.B. Meyer, M. Meyer, M. Missiroli, J. Mnich, V. Myronenko, S.K. Pflitsch, D. Pitzl, A. Raspereza, P. Saxena, P. Schütze, C. Schwanenberger, R. Shevchenko, A. Singh, H. Tholen, O. Turkot, A. Vagnerini, G.P. Van Onsem, R. Walsh, Y. Wen, K. Wichmann, C. Wissing, O. Zenaiev

University of Hamburg, Hamburg, Germany

R. Aggleton, S. Bein, L. Benato, A. Benecke, V. Blobel, T. Dreyer, A. Ebrahimi, E. Garutti, D. Gonzalez, P. Gunnellini, J. Haller, A. Hinzmann, A. Karavdina, G. Kasieczka, R. Klanner, R. Kogler, N. Kovalchuk, S. Kurz, V. Kutzner, J. Lange, D. Marconi, J. Multhaup, M. Niedziela, C.E.N. Niemeyer, D. Nowatschin, A. Perieanu, A. Reimers, O. Rieger, C. Scharf, P. Schleper, S. Schumann, J. Schwandt, J. Sonneveld, H. Stadie, G. Steinbrück, F.M. Stober, M. Stöver, B. Vormwald, I. Zoi

Karlsruher Institut fuer Technologie, Karlsruhe, Germany

M. Akbiyik, C. Barth, M. Baselga, S. Baur, E. Butz, R. Caspart, T. Chwalek, F. Colombo, W. De Boer, A. Dierlamm, K. El Morabit, N. Faltermann, B. Freund, M. Giffels, M.A. Harrendorf, F. Hartmann[17], S.M. Heindl, U. Husemann, I. Katkov[15], S. Kudella, S. Mitra, M.U. Mozer, Th. Müller, M. Musich, M. Plagge, G. Quast, K. Rabbertz, M. Schröder, I. Shvetsov, H.J. Simonis, R. Ulrich, S. Wayand, M. Weber, T. Weiler, C. Wöhrmann, R. Wolf

Institute of Nuclear and Particle Physics (INPP), NCSR Demokritos, Aghia Paraskevi, Greece

G. Anagnostou, G. Daskalakis, T. Geralis, A. Kyriakis, D. Loukas, G. Paspalaki

National and Kapodistrian University of Athens, Athens, Greece

A. Agapitos, G. Karathanasis, P. Kontaxakis, A. Panagiotou, I. Papavergou, N. Saoulidou, E. Tziaferi, K. Vellidis

National Technical University of Athens, Athens, Greece

K. Kousouris, I. Papakrivopoulos, G. Tsipolitis

University of Ioánnina, Ioánnina, Greece

I. Evangelou, C. Foudas, P. Gianneios, P. Katsoulis, P. Kokkas, S. Mallios, N. Manthos, I. Papadopoulos, E. Paradas, J. Strologas, F.A. Triantis, D. Tsitsonis

MTA-ELTE Lendület CMS Particle and Nuclear Physics Group, Eötvös Loránd University, Budapest, Hungary

M. Bartók[21], M. Csanad, N. Filipovic, P. Major, M.I. Nagy, G. Pasztor, O. Surányi, G.I. Veres

Wigner Research Centre for Physics, Budapest, Hungary

G. Bencze, C. Hajdu, D. Horvath[22], Á. Hunyadi, F. Sikler, T.Á. Vámi, V. Veszpremi, G. Vesztergombi[†]

Institute of Nuclear Research ATOMKI, Debrecen, Hungary

N. Beni, S. Czellar, J. Karancsi[21], A. Makovec, J. Molnar, Z. Szillasi

Institute of Physics, University of Debrecen, Debrecen, Hungary

P. Raics, Z.L. Trocsanyi, B. Ujvari

Indian Institute of Science (IISc), Bangalore, India

S. Choudhury, J.R. Komaragiri, P.C. Tiwari

National Institute of Science Education and Research, HBNI, Bhubaneswar, India

S. Bahinipati[24], C. Kar, P. Mal, K. Mandal, A. Nayak[25], D.K. Sahoo[24], S.K. Swain

Panjab University, Chandigarh, India

S. Bansal, S.B. Beri, V. Bhatnagar, S. Chauhan, R. Chawla, N. Dhingra, R. Gupta, A. Kaur, M. Kaur, S. Kaur, P. Kumari, M. Lohan, A. Mehta, K. Sandeep, S. Sharma, J.B. Singh, A.K. Virdi, G. Walia

University of Delhi, Delhi, India

A. Bhardwaj, B.C. Choudhary, R.B. Garg, M. Gola, S. Keshri, Ashok Kumar, S. Malhotra, M. Naimuddin, P. Priyanka, K. Ranjan, Aashaq Shah, R. Sharma

Saha Institute of Nuclear Physics, HBNI, Kolkata, India

R. Bhardwaj[26], M. Bharti[26], R. Bhattacharya, S. Bhattacharya, U. Bhawandeep[26], D. Bhowmik, S. Dey, S. Dutt[26], S. Dutta, S. Ghosh, K. Mondal, S. Nandan, A. Purohit, P.K. Rout, A. Roy, S. Roy Chowdhury, G. Saha, S. Sarkar, M. Sharan, B. Singh[26], S. Thakur[26]

Indian Institute of Technology Madras, Madras, India

P.K. Behera

Bhabha Atomic Research Centre, Mumbai, India

R. Chudasama, D. Dutta, V. Jha, V. Kumar, D.K. Mishra, P.K. Netrakanti, L.M. Pant, P. Shukla

Tata Institute of Fundamental Research-A, Mumbai, India

T. Aziz, M.A. Bhat, S. Dugad, G.B. Mohanty, N. Sur, B. Sutar, RavindraKumar Verma

Tata Institute of Fundamental Research-B, Mumbai, India

S. Banerjee, S. Bhattacharya, S. Chatterjee, P. Das, M. Guchait, Sa. Jain, S. Karmakar, S. Kumar, M. Maity[27], G. Majumder, K. Mazumdar, N. Sahoo, T. Sarkar[27]

Indian Institute of Science Education and Research (IISER), Pune, India

S. Chauhan, S. Dube, V. Hegde, A. Kapoor, K. Kothekar, S. Pandey, A. Rane, A. Rastogi, S. Sharma

Institute for Research in Fundamental Sciences (IPM), Tehran, Iran

S. Chenarani[28], E. Eskandari Tadavani, S.M. Etesami[28], M. Khakzad, M. Mohammadi Najafabadi, M. Naseri, F. Rezaei Hosseinabadi, B. Safarzadeh[29], M. Zeinali

University College Dublin, Dublin, Ireland

M. Felcini, M. Grunewald

INFN Sezione di Bari [a], Università di Bari [b], Politecnico di Bari [c], Bari, Italy

M. Abbrescia[a,b], C. Calabria[a,b], A. Colaleo[a], D. Creanza[a,c], L. Cristella[a,b], N. De Filippis[a,c], M. De Palma[a,b], A. Di Florio[a,b], F. Errico[a,b], L. Fiore[a], A. Gelmi[a,b], G. Iaselli[a,c], M. Ince[a,b], S. Lezki[a,b], G. Maggi[a,c], M. Maggi[a], G. Miniello[a,b], S. My[a,b], S. Nuzzo[a,b], A. Pompili[a,b], G. Pugliese[a,c], R. Radogna[a], A. Ranieri[a], G. Selvaggi[a,b], A. Sharma[a], L. Silvestris[a], R. Venditti[a], P. Verwilligen[a], G. Zito[a]

INFN Sezione di Bologna [a], Università di Bologna [b], Bologna, Italy

G. Abbiendi[a], C. Battilana[a,b], D. Bonacorsi[a,b], L. Borgonovi[a,b], S. Braibant-Giacomelli[a,b], R. Campanini[a,b], P. Capiluppi[a,b], A. Castro[a,b], F.R. Cavallo[a], S.S. Chhibra[a,b], C. Ciocca[a], G. Codispoti[a,b], M. Cuffiani[a,b], G.M. Dallavalle[a], F. Fabbri[a], A. Fanfani[a,b], E. Fontanesi, P. Giacomelli[a], C. Grandi[a], L. Guiducci[a,b], F. Iemmi[a,b], S. Marcellini[a], G. Masetti[a], A. Montanari[a], F.L. Navarria[a,b], A. Perrotta[a], F. Primavera[a,b,17], A.M. Rossi[a,b], T. Rovelli[a,b], G.P. Siroli[a,b], N. Tosi[a]

INFN Sezione di Catania [a], Università di Catania [b], Catania, Italy

S. Albergo[a,b], A. Di Mattia[a], R. Potenza[a,b], A. Tricomi[a,b], C. Tuve[a,b]

INFN Sezione di Firenze [a], Università di Firenze [b], Firenze, Italy

G. Barbagli[a], K. Chatterjee[a,b], V. Ciulli[a,b], C. Civinini[a], R. D'Alessandro[a,b], E. Focardi[a,b], G. Latino, P. Lenzi[a,b], M. Meschini[a], S. Paoletti[a], L. Russo[a,30], G. Sguazzoni[a], D. Strom[a], L. Viliani[a]

INFN Laboratori Nazionali di Frascati, Frascati, Italy

L. Benussi, S. Bianco, F. Fabbri, D. Piccolo

INFN Sezione di Genova [a], Università di Genova [b], Genova, Italy

F. Ferro[a], R. Mulargia[a,b], F. Ravera[a,b], E. Robutti[a], S. Tosi[a,b]

INFN Sezione di Milano-Bicocca [a], Università di Milano-Bicocca [b], Milano, Italy

A. Benaglia[a], A. Beschi[b], F. Brivio[a,b], V. Ciriolo[a,b,17], S. Di Guida[a,d,17], M.E. Dinardo[a,b], S. Fiorendi[a,b], S. Gennai[a], A. Ghezzi[a,b], P. Govoni[a,b], M. Malberti[a,b], S. Malvezzi[a], D. Menasce[a],

F. Monti, L. Moroni^a, M. Paganoni^{a,b}, D. Pedrini^a, S. Ragazzi^{a,b}, T. Tabarelli de Fatis^{a,b}, D. Zuolo^{a,b}

INFN Sezione di Napoli ^{a}, Università di Napoli 'Federico II' ^{b}, Napoli, Italy, Università della Basilicata ^{c}, Potenza, Italy, Università G. Marconi ^{d}, Roma, Italy

S. Buontempo^a, N. Cavallo^{a,c}, A. De Iorio^{a,b}, A. Di Crescenzo^{a,b}, F. Fabozzi^{a,c}, F. Fienga^a, G. Galati^a, A.O.M. Iorio^{a,b}, W.A. Khan^a, L. Lista^a, S. Meola^{a,d,17}, P. Paolucci^{a,17}, C. Sciacca^{a,b}, E. Voevodina^{a,b}

INFN Sezione di Padova ^{a}, Università di Padova ^{b}, Padova, Italy, Università di Trento ^{c}, Trento, Italy

P. Azzi^a, N. Bacchetta^a, D. Bisello^{a,b}, A. Boletti^{a,b}, A. Bragagnolo, R. Carlin^{a,b}, P. Checchia^a, M. Dall'Osso^{a,b}, P. De Castro Manzano^a, T. Dorigo^a, U. Dosselli^a, F. Gasparini^{a,b}, U. Gasparini^{a,b}, A. Gozzelino^a, S.Y. Hoh, S. Lacaprara^a, P. Lujan, M. Margoni^{a,b}, A.T. Meneguzzo^{a,b}, J. Pazzini^{a,b}, M. Presilla^b, P. Ronchese^{a,b}, R. Rossin^{a,b}, F. Simonetto^{a,b}, A. Tiko, E. Torassa^a, M. Tosi^{a,b}, M. Zanetti^{a,b}, P. Zotto^{a,b}, G. Zumerle^{a,b}

INFN Sezione di Pavia ^{a}, Università di Pavia ^{b}, Pavia, Italy

A. Braghieri^a, A. Magnani^a, P. Montagna^{a,b}, S.P. Ratti^{a,b}, V. Re^a, M. Ressegotti^{a,b}, C. Riccardi^{a,b}, P. Salvini^a, I. Vai^{a,b}, P. Vitulo^{a,b}

INFN Sezione di Perugia ^{a}, Università di Perugia ^{b}, Perugia, Italy

M. Biasini^{a,b}, G.M. Bilei^a, C. Cecchi^{a,b}, D. Ciangottini^{a,b}, L. Fanò^{a,b}, P. Lariccia^{a,b}, R. Leonardi^{a,b}, E. Manoni^a, G. Mantovani^{a,b}, V. Mariani^{a,b}, M. Menichelli^a, A. Rossi^{a,b}, A. Santocchia^{a,b}, D. Spiga^a

INFN Sezione di Pisa ^{a}, Università di Pisa ^{b}, Scuola Normale Superiore di Pisa ^{c}, Pisa, Italy

K. Androsov^a, P. Azzurri^a, G. Bagliesi^a, L. Bianchini^a, T. Boccali^a, L. Borrello, R. Castaldi^a, M.A. Ciocci^{a,b}, R. Dell'Orso^a, G. Fedi^a, F. Fiori^{a,c}, L. Giannini^{a,c}, A. Giassi^a, M.T. Grippo^a, F. Ligabue^{a,c}, E. Manca^{a,c}, G. Mandorli^{a,c}, A. Messineo^{a,b}, F. Palla^a, A. Rizzi^{a,b}, G. Rolandi^{31}, P. Spagnolo^a, R. Tenchini^a, G. Tonelli^{a,b}, A. Venturi^a, P.G. Verdini^a

INFN Sezione di Roma ^{a}, Sapienza Università di Roma ^{b}, Rome, Italy

L. Barone^{a,b}, F. Cavallari^a, M. Cipriani^{a,b}, D. Del Re^{a,b}, E. Di Marco^{a,b}, M. Diemoz^a, S. Gelli^{a,b}, E. Longo^{a,b}, B. Marzocchi^{a,b}, P. Meridiani^a, G. Organtini^{a,b}, F. Pandolfi^a, R. Paramatti^{a,b}, F. Preiato^{a,b}, S. Rahatlou^{a,b}, C. Rovelli^a, F. Santanastasio^{a,b}

INFN Sezione di Torino ^{a}, Università di Torino ^{b}, Torino, Italy, Università del Piemonte Orientale ^{c}, Novara, Italy

N. Amapane^{a,b}, R. Arcidiacono^{a,c}, S. Argiro^{a,b}, M. Arneodo^{a,c}, N. Bartosik^a, R. Bellan^{a,b}, C. Biino^a, A. Cappati^{a,b}, N. Cartiglia^a, F. Cenna^{a,b}, S. Cometti^a, M. Costa^{a,b}, R. Covarelli^{a,b}, N. Demaria^a, B. Kiani^{a,b}, C. Mariotti^a, S. Maselli^a, E. Migliore^{a,b}, V. Monaco^{a,b}, E. Monteil^{a,b}, M. Monteno^a, M.M. Obertino^{a,b}, L. Pacher^{a,b}, N. Pastrone^a, M. Pelliccioni^a, G.L. Pinna Angioni^{a,b}, A. Romero^{a,b}, M. Ruspa^{a,c}, R. Sacchi^{a,b}, R. Salvatico^{a,b}, K. Shchelina^{a,b}, V. Sola^a, A. Solano^{a,b}, D. Soldi^{a,b}, A. Staiano^a

INFN Sezione di Trieste ^{a}, Università di Trieste ^{b}, Trieste, Italy

S. Belforte^a, V. Candelise^{a,b}, M. Casarsa^a, F. Cossutti^a, A. Da Rold^{a,b}, G. Della Ricca^{a,b}, F. Vazzoler^{a,b}, A. Zanetti^a

Kyungpook National University, Daegu, Korea

D.H. Kim, G.N. Kim, M.S. Kim, J. Lee, S. Lee, S.W. Lee, C.S. Moon, Y.D. Oh, S.I. Pak, S. Sekmen, D.C. Son, Y.C. Yang

Chonnam National University, Institute for Universe and Elementary Particles, Kwangju, Korea

H. Kim, D.H. Moon, G. Oh

Hanyang University, Seoul, Korea

B. Francois, J. Goh[32], T.J. Kim

Korea University, Seoul, Korea

S. Cho, S. Choi, Y. Go, D. Gyun, S. Ha, B. Hong, Y. Jo, K. Lee, K.S. Lee, S. Lee, J. Lim, S.K. Park, Y. Roh

Sejong University, Seoul, Korea

H.S. Kim

Seoul National University, Seoul, Korea

J. Almond, J. Kim, J.S. Kim, H. Lee, K. Lee, K. Nam, S.B. Oh, B.C. Radburn-Smith, S.h. Seo, U.K. Yang, H.D. Yoo, G.B. Yu

University of Seoul, Seoul, Korea

D. Jeon, H. Kim, J.H. Kim, J.S.H. Lee, I.C. Park

Sungkyunkwan University, Suwon, Korea

Y. Choi, C. Hwang, J. Lee, I. Yu

Vilnius University, Vilnius, Lithuania

V. Dudenas, A. Juodagalvis, J. Vaitkus

National Centre for Particle Physics, Universiti Malaya, Kuala Lumpur, Malaysia

I. Ahmed, Z.A. Ibrahim, M.A.B. Md Ali[33], F. Mohamad Idris[34], W.A.T. Wan Abdullah, M.N. Yusli, Z. Zolkapli

Universidad de Sonora (UNISON), Hermosillo, Mexico

J.F. Benitez, A. Castaneda Hernandez, J.A. Murillo Quijada

Centro de Investigacion y de Estudios Avanzados del IPN, Mexico City, Mexico

H. Castilla-Valdez, E. De La Cruz-Burelo, M.C. Duran-Osuna, I. Heredia-De La Cruz[35], R. Lopez-Fernandez, J. Mejia Guisao, R.I. Rabadan-Trejo, M. Ramirez-Garcia, G. Ramirez-Sanchez, R. Reyes-Almanza, A. Sanchez-Hernandez

Universidad Iberoamericana, Mexico City, Mexico

S. Carrillo Moreno, C. Oropeza Barrera, F. Vazquez Valencia

Benemerita Universidad Autonoma de Puebla, Puebla, Mexico

J. Eysermans, I. Pedraza, H.A. Salazar Ibarguen, C. Uribe Estrada

Universidad Autónoma de San Luis Potosí, San Luis Potosí, Mexico

A. Morelos Pineda

University of Auckland, Auckland, New Zealand

D. Krofcheck

University of Canterbury, Christchurch, New Zealand

S. Bheesette, P.H. Butler

National Centre for Physics, Quaid-I-Azam University, Islamabad, Pakistan

A. Ahmad, M. Ahmad, M.I. Asghar, Q. Hassan, H.R. Hoorani, A. Saddique, M.A. Shah, M. Shoaib, M. Waqas

National Centre for Nuclear Research, Swierk, Poland

H. Bialkowska, M. Bluj, B. Boimska, T. Frueboes, M. Górski, M. Kazana, M. Szleper, P. Traczyk, P. Zalewski

Institute of Experimental Physics, Faculty of Physics, University of Warsaw, Warsaw, Poland

K. Bunkowski, A. Byszuk[36], K. Doroba, A. Kalinowski, M. Konecki, J. Krolikowski, M. Misiura, M. Olszewski, A. Pyskir, M. Walczak

Laboratório de Instrumentação e Física Experimental de Partículas, Lisboa, Portugal

M. Araujo, P. Bargassa, C. Beirão Da Cruz E Silva, A. Di Francesco, P. Faccioli, B. Galinhas, M. Gallinaro, J. Hollar, N. Leonardo, J. Seixas, G. Strong, O. Toldaiev, J. Varela

Joint Institute for Nuclear Research, Dubna, Russia

S. Afanasiev, P. Bunin, M. Gavrilenko, I. Golutvin, I. Gorbunov, A. Kamenev, V. Karjavine, A. Lanev, A. Malakhov, V. Matveev[37,38], P. Moisenz, V. Palichik, V. Perelygin, S. Shmatov, S. Shulha, N. Skatchkov, V. Smirnov, N. Voytishin, A. Zarubin

Petersburg Nuclear Physics Institute, Gatchina (St. Petersburg), Russia

V. Golovtsov, Y. Ivanov, V. Kim[39], E. Kuznetsova[40], P. Levchenko, V. Murzin, V. Oreshkin, I. Smirnov, D. Sosnov, V. Sulimov, L. Uvarov, S. Vavilov, A. Vorobyev

Institute for Nuclear Research, Moscow, Russia

Yu. Andreev, A. Dermenev, S. Gninenko, N. Golubev, A. Karneyeu, M. Kirsanov, N. Krasnikov, A. Pashenkov, D. Tlisov, A. Toropin

Institute for Theoretical and Experimental Physics, Moscow, Russia

V. Epshteyn, V. Gavrilov, N. Lychkovskaya, V. Popov, I. Pozdnyakov, G. Safronov, A. Spiridonov, A. Stepennov, V. Stolin, M. Toms, E. Vlasov, A. Zhokin

Moscow Institute of Physics and Technology, Moscow, Russia

T. Aushev

National Research Nuclear University 'Moscow Engineering Physics Institute' (MEPhI), Moscow, Russia

M. Chadeeva[41], P. Parygin, D. Philippov, S. Polikarpov[41], E. Popova, V. Rusinov

P.N. Lebedev Physical Institute, Moscow, Russia

V. Andreev, M. Azarkin, I. Dremin[38], M. Kirakosyan, A. Terkulov

Skobeltsyn Institute of Nuclear Physics, Lomonosov Moscow State University, Moscow, Russia

A. Baskakov, A. Belyaev, E. Boos, M. Dubinin[42], L. Dudko, A. Ershov, A. Gribushin, A. Kaminskiy[43], V. Klyukhin, O. Kodolova, I. Lokhtin, I. Miagkov, S. Obraztsov, S. Petrushanko, V. Savrin

Novosibirsk State University (NSU), Novosibirsk, Russia

A. Barnyakov[44], V. Blinov[44], T. Dimova[44], L. Kardapoltsev[44], Y. Skovpen[44]

Institute for High Energy Physics of National Research Centre 'Kurchatov Institute', Protvino, Russia

I. Azhgirey, I. Bayshev, S. Bitioukov, V. Kachanov, A. Kalinin, D. Konstantinov, P. Mandrik, V. Petrov, R. Ryutin, S. Slabospitskii, A. Sobol, S. Troshin, N. Tyurin, A. Uzunian, A. Volkov

National Research Tomsk Polytechnic University, Tomsk, Russia

A. Babaev, S. Baidali, V. Okhotnikov

University of Belgrade: Faculty of Physics and VINCA Institute of Nuclear Sciences

P. Adzic[45], P. Cirkovic, D. Devetak, M. Dordevic, J. Milosevic

Centro de Investigaciones Energéticas Medioambientales y Tecnológicas (CIEMAT), Madrid, Spain

J. Alcaraz Maestre, A. Álvarez Fernández, I. Bachiller, M. Barrio Luna, J.A. Brochero Cifuentes, M. Cerrada, N. Colino, B. De La Cruz, A. Delgado Peris, C. Fernandez Bedoya, J.P. Fernández Ramos, J. Flix, M.C. Fouz, O. Gonzalez Lopez, S. Goy Lopez, J.M. Hernandez, M.I. Josa, D. Moran, A. Pérez-Calero Yzquierdo, J. Puerta Pelayo, I. Redondo, L. Romero, M.S. Soares, A. Triossi

Universidad Autónoma de Madrid, Madrid, Spain

C. Albajar, J.F. de Trocóniz

Universidad de Oviedo, Oviedo, Spain

J. Cuevas, C. Erice, J. Fernandez Menendez, S. Folgueras, I. Gonzalez Caballero, J.R. González Fernández, E. Palencia Cortezon, V. Rodríguez Bouza, S. Sanchez Cruz, J.M. Vizan Garcia

Instituto de Física de Cantabria (IFCA), CSIC-Universidad de Cantabria, Santander, Spain

I.J. Cabrillo, A. Calderon, B. Chazin Quero, J. Duarte Campderros, M. Fernandez, P.J. Fernández Manteca, A. García Alonso, J. Garcia-Ferrero, G. Gomez, A. Lopez Virto, J. Marco, C. Martinez Rivero, P. Martinez Ruiz del Arbol, F. Matorras, J. Piedra Gomez, C. Prieels, T. Rodrigo, A. Ruiz-Jimeno, L. Scodellaro, N. Trevisani, I. Vila, R. Vilar Cortabitarte

University of Ruhuna, Department of Physics, Matara, Sri Lanka

N. Wickramage

CERN, European Organization for Nuclear Research, Geneva, Switzerland

D. Abbaneo, B. Akgun, E. Auffray, G. Auzinger, P. Baillon, A.H. Ball, D. Barney, J. Bendavid, M. Bianco, A. Bocci, C. Botta, E. Brondolin, T. Camporesi, M. Cepeda, G. Cerminara, E. Chapon, Y. Chen, G. Cucciati, D. d'Enterria, A. Dabrowski, N. Daci, V. Daponte, A. David, A. De Roeck, N. Deelen, M. Dobson, M. Dünser, N. Dupont, A. Elliott-Peisert, P. Everaerts, F. Fallavollita[46], D. Fasanella, G. Franzoni, J. Fulcher, W. Funk, D. Gigi, A. Gilbert, K. Gill, F. Glege, M. Gruchala, M. Guilbaud, D. Gulhan, J. Hegeman, C. Heidegger, V. Innocente, A. Jafari, P. Janot, O. Karacheban[20], J. Kieseler, A. Kornmayer, M. Krammer[1], C. Lange, P. Lecoq, C. Lourenço, L. Malgeri, M. Mannelli, A. Massironi, F. Meijers, J.A. Merlin, S. Mersi, E. Meschi, P. Milenovic[47], F. Moortgat, M. Mulders, J. Ngadiuba, S. Nourbakhsh, S. Orfanelli, L. Orsini, F. Pantaleo[17], L. Pape, E. Perez, M. Peruzzi, A. Petrilli, G. Petrucciani, A. Pfeiffer, M. Pierini, F.M. Pitters, D. Rabady, A. Racz, T. Reis, M. Rovere, H. Sakulin, C. Schäfer, C. Schwick, M. Selvaggi, A. Sharma, P. Silva, P. Sphicas[48], A. Stakia, J. Steggemann, D. Treille, A. Tsirou, V. Veckalns[49], M. Verzetti, W.D. Zeuner

Paul Scherrer Institut, Villigen, Switzerland

L. Caminada[50], K. Deiters, W. Erdmann, R. Horisberger, Q. Ingram, H.C. Kaestli, D. Kotlinski, U. Langenegger, T. Rohe, S.A. Wiederkehr

ETH Zurich - Institute for Particle Physics and Astrophysics (IPA), Zurich, Switzerland

M. Backhaus, L. Bäni, P. Berger, N. Chernyavskaya, G. Dissertori, M. Dittmar, M. Donegà, C. Dorfer, T.A. Gómez Espinosa, C. Grab, D. Hits, T. Klijnsma, W. Lustermann, R.A. Manzoni, M. Marionneau, M.T. Meinhard, F. Micheli, P. Musella, F. Nessi-Tedaldi, J. Pata, F. Pauss, G. Perrin, L. Perrozzi, S. Pigazzini, M. Quittnat, C. Reissel, D. Ruini, D.A. Sanz Becerra, M. Schönenberger, L. Shchutska, V.R. Tavolaro, K. Theofilatos, M.L. Vesterbacka Olsson, R. Wallny, D.H. Zhu

Universität Zürich, Zurich, Switzerland

T.K. Aarrestad, C. Amsler[51], D. Brzhechko, M.F. Canelli, A. De Cosa, R. Del Burgo, S. Donato, C. Galloni, T. Hreus, B. Kilminster, S. Leontsinis, I. Neutelings, G. Rauco, P. Robmann, D. Salerno, K. Schweiger, C. Seitz, Y. Takahashi, A. Zucchetta

National Central University, Chung-Li, Taiwan

T.H. Doan, R. Khurana, C.M. Kuo, W. Lin, A. Pozdnyakov, S.S. Yu

National Taiwan University (NTU), Taipei, Taiwan

P. Chang, Y. Chao, K.F. Chen, P.H. Chen, W.-S. Hou, Arun Kumar, Y.F. Liu, R.-S. Lu, E. Paganis, A. Psallidas, A. Steen

Chulalongkorn University, Faculty of Science, Department of Physics, Bangkok, Thailand

B. Asavapibhop, N. Srimanobhas, N. Suwonjandee

Çukurova University, Physics Department, Science and Art Faculty, Adana, Turkey

M.N. Bakirci[52], A. Bat, F. Boran, S. Cerci[53], S. Damarseckin, Z.S. Demiroglu, F. Dolek, C. Dozen, E. Eskut, S. Girgis, G. Gokbulut, Y. Guler, E. Gurpinar, I. Hos[54], C. Isik, E.E. Kangal[55], O. Kara, U. Kiminsu, M. Oglakci, G. Onengut, K. Ozdemir[56], A. Polatoz, D. Sunar Cerci[53], U.G. Tok, H. Topakli[52], S. Turkcapar, I.S. Zorbakir, C. Zorbilmez

Middle East Technical University, Physics Department, Ankara, Turkey

B. Isildak[57], G. Karapinar[58], M. Yalvac, M. Zeyrek

Bogazici University, Istanbul, Turkey

I.O. Atakisi, E. Gülmez, M. Kaya[59], O. Kaya[60], S. Ozkorucuklu[61], S. Tekten, E.A. Yetkin[62]

Istanbul Technical University, Istanbul, Turkey

M.N. Agaras, A. Cakir, K. Cankocak, Y. Komurcu, S. Sen[63]

Institute for Scintillation Materials of National Academy of Science of Ukraine, Kharkov, Ukraine

B. Grynyov

National Scientific Center, Kharkov Institute of Physics and Technology, Kharkov, Ukraine

L. Levchuk

University of Bristol, Bristol, United Kingdom

F. Ball, J.J. Brooke, D. Burns, E. Clement, D. Cussans, O. Davignon, H. Flacher, J. Goldstein, G.P. Heath, H.F. Heath, L. Kreczko, D.M. Newbold[64], S. Paramesvaran, B. Penning, T. Sakuma, D. Smith, V.J. Smith, J. Taylor, A. Titterton

Rutherford Appleton Laboratory, Didcot, United Kingdom

K.W. Bell, A. Belyaev[65], C. Brew, R.M. Brown, D. Cieri, D.J.A. Cockerill, J.A. Coughlan, K. Harder, S. Harper, J. Linacre, K. Manolopoulos, E. Olaiya, D. Petyt, C.H. Shepherd-Themistocleous, A. Thea, I.R. Tomalin, T. Williams, W.J. Womersley

Imperial College, London, United Kingdom

R. Bainbridge, P. Bloch, J. Borg, S. Breeze, O. Buchmuller, A. Bundock, D. Colling, P. Dauncey, G. Davies, M. Della Negra, R. Di Maria, G. Hall, G. Iles, T. James, M. Komm, C. Laner, L. Lyons, A.-M. Magnan, S. Malik, A. Martelli, J. Nash[66], A. Nikitenko[7], V. Palladino, M. Pesaresi, D.M. Raymond, A. Richards, A. Rose, E. Scott, C. Seez, A. Shtipliyski, G. Singh, M. Stoye, T. Strebler, S. Summers, A. Tapper, K. Uchida, T. Virdee[17], N. Wardle, D. Winterbottom, J. Wright, S.C. Zenz

Brunel University, Uxbridge, United Kingdom

J.E. Cole, P.R. Hobson, A. Khan, P. Kyberd, C.K. Mackay, A. Morton, I.D. Reid, L. Teodorescu, S. Zahid

Baylor University, Waco, U.S.A.

K. Call, J. Dittmann, K. Hatakeyama, H. Liu, C. Madrid, B. McMaster, N. Pastika, C. Smith

Catholic University of America, Washington, DC, U.S.A.

R. Bartek, A. Dominguez

The University of Alabama, Tuscaloosa, U.S.A.

A. Buccilli, S.I. Cooper, C. Henderson, P. Rumerio, C. West

Boston University, Boston, U.S.A.

D. Arcaro, T. Bose, D. Gastler, D. Pinna, D. Rankin, C. Richardson, J. Rohlf, L. Sulak, D. Zou

Brown University, Providence, U.S.A.

G. Benelli, X. Coubez, D. Cutts, M. Hadley, J. Hakala, U. Heintz, J.M. Hogan[67], K.H.M. Kwok, E. Laird, G. Landsberg, J. Lee, Z. Mao, M. Narain, S. Sagir[68], R. Syarif, E. Usai, D. Yu

University of California, Davis, Davis, U.S.A.

R. Band, C. Brainerd, R. Breedon, D. Burns, M. Calderon De La Barca Sanchez, M. Chertok, J. Conway, R. Conway, P.T. Cox, R. Erbacher, C. Flores, G. Funk, W. Ko, O. Kukral, R. Lander, M. Mulhearn, D. Pellett, J. Pilot, S. Shalhout, M. Shi, D. Stolp, D. Taylor, K. Tos, M. Tripathi, Z. Wang, F. Zhang

University of California, Los Angeles, U.S.A.

M. Bachtis, C. Bravo, R. Cousins, A. Dasgupta, A. Florent, J. Hauser, M. Ignatenko, N. Mccoll, S. Regnard, D. Saltzberg, C. Schnaible, V. Valuev

University of California, Riverside, Riverside, U.S.A.

E. Bouvier, K. Burt, R. Clare, J.W. Gary, S.M.A. Ghiasi Shirazi, G. Hanson, G. Karapostoli, E. Kennedy, F. Lacroix, O.R. Long, M. Olmedo Negrete, M.I. Paneva, W. Si, L. Wang, H. Wei, S. Wimpenny, B.R. Yates

University of California, San Diego, La Jolla, U.S.A.

J.G. Branson, P. Chang, S. Cittolin, M. Derdzinski, R. Gerosa, D. Gilbert, B. Hashemi, A. Holzner, D. Klein, G. Kole, V. Krutelyov, J. Letts, M. Masciovecchio, D. Olivito, S. Padhi, M. Pieri, M. Sani, V. Sharma, S. Simon, M. Tadel, A. Vartak, S. Wasserbaech[69], J. Wood, F. Würthwein, A. Yagil, G. Zevi Della Porta

University of California, Santa Barbara - Department of Physics, Santa Barbara, U.S.A.

N. Amin, R. Bhandari, C. Campagnari, M. Citron, V. Dutta, M. Franco Sevilla, L. Gouskos, R. Heller, J. Incandela, H. Mei, A. Ovcharova, H. Qu, J. Richman, D. Stuart, I. Suarez, S. Wang, J. Yoo

California Institute of Technology, Pasadena, U.S.A.

D. Anderson, A. Bornheim, J.M. Lawhorn, N. Lu, H.B. Newman, T.Q. Nguyen, M. Spiropulu, J.R. Vlimant, R. Wilkinson, S. Xie, Z. Zhang, R.Y. Zhu

Carnegie Mellon University, Pittsburgh, U.S.A.

M.B. Andrews, T. Ferguson, T. Mudholkar, M. Paulini, M. Sun, I. Vorobiev, M. Weinberg

University of Colorado Boulder, Boulder, U.S.A.

J.P. Cumalat, W.T. Ford, F. Jensen, A. Johnson, E. MacDonald, T. Mulholland, R. Patel, A. Perloff, K. Stenson, K.A. Ulmer, S.R. Wagner

Cornell University, Ithaca, U.S.A.

J. Alexander, J. Chaves, Y. Cheng, J. Chu, A. Datta, K. Mcdermott, N. Mirman, J.R. Patterson, D. Quach, A. Rinkevicius, A. Ryd, L. Skinnari, L. Soffi, S.M. Tan, Z. Tao, J. Thom, J. Tucker, P. Wittich, M. Zientek

Fermi National Accelerator Laboratory, Batavia, U.S.A.

S. Abdullin, M. Albrow, M. Alyari, G. Apollinari, A. Apresyan, A. Apyan, S. Banerjee, L.A.T. Bauerdick, A. Beretvas, J. Berryhill, P.C. Bhat, K. Burkett, J.N. Butler, A. Canepa,

G.B. Cerati, H.W.K. Cheung, F. Chlebana, M. Cremonesi, J. Duarte, V.D. Elvira, J. Freeman, Z. Gecse, E. Gottschalk, L. Gray, D. Green, S. Grünendahl, O. Gutsche, J. Hanlon, R.M. Harris, S. Hasegawa, J. Hirschauer, Z. Hu, B. Jayatilaka, S. Jindariani, M. Johnson, U. Joshi, B. Klima, M.J. Kortelainen, B. Kreis, S. Lammel, D. Lincoln, R. Lipton, M. Liu, T. Liu, J. Lykken, K. Maeshima, J.M. Marraffino, D. Mason, P. McBride, P. Merkel, S. Mrenna, S. Nahn, V. O'Dell, K. Pedro, C. Pena, O. Prokofyev, G. Rakness, L. Ristori, A. Savoy-Navarro[70], B. Schneider, E. Sexton-Kennedy, A. Soha, W.J. Spalding, L. Spiegel, S. Stoynev, J. Strait, N. Strobbe, L. Taylor, S. Tkaczyk, N.V. Tran, L. Uplegger, E.W. Vaandering, C. Vernieri, M. Verzocchi, R. Vidal, M. Wang, H.A. Weber, A. Whitbeck

University of Florida, Gainesville, U.S.A.

D. Acosta, P. Avery, P. Bortignon, D. Bourilkov, A. Brinkerhoff, L. Cadamuro, A. Carnes, D. Curry, R.D. Field, S.V. Gleyzer, B.M. Joshi, J. Konigsberg, A. Korytov, K.H. Lo, P. Ma, K. Matchev, G. Mitselmakher, D. Rosenzweig, K. Shi, D. Sperka, J. Wang, S. Wang, X. Zuo

Florida International University, Miami, U.S.A.

Y.R. Joshi, S. Linn

Florida State University, Tallahassee, U.S.A.

A. Ackert, T. Adams, A. Askew, S. Hagopian, V. Hagopian, K.F. Johnson, T. Kolberg, G. Martinez, T. Perry, H. Prosper, A. Saha, C. Schiber, R. Yohay

Florida Institute of Technology, Melbourne, U.S.A.

M.M. Baarmand, V. Bhopatkar, S. Colafranceschi, M. Hohlmann, D. Noonan, M. Rahmani, T. Roy, F. Yumiceva

University of Illinois at Chicago (UIC), Chicago, U.S.A.

M.R. Adams, L. Apanasevich, D. Berry, R.R. Betts, R. Cavanaugh, X. Chen, S. Dittmer, O. Evdokimov, C.E. Gerber, D.A. Hangal, D.J. Hofman, K. Jung, J. Kamin, C. Mills, M.B. Tonjes, N. Varelas, H. Wang, X. Wang, Z. Wu, J. Zhang

The University of Iowa, Iowa City, U.S.A.

M. Alhusseini, B. Bilki[71], W. Clarida, K. Dilsiz[72], S. Durgut, R.P. Gandrajula, M. Haytmyradov, V. Khristenko, J.-P. Merlo, A. Mestvirishvili, A. Moeller, J. Nachtman, H. Ogul[73], Y. Onel, F. Ozok[74], A. Penzo, C. Snyder, E. Tiras, J. Wetzel

Johns Hopkins University, Baltimore, U.S.A.

B. Blumenfeld, A. Cocoros, N. Eminizer, D. Fehling, L. Feng, A.V. Gritsan, W.T. Hung, P. Maksimovic, J. Roskes, U. Sarica, M. Swartz, M. Xiao, C. You

The University of Kansas, Lawrence, U.S.A.

A. Al-bataineh, P. Baringer, A. Bean, S. Boren, J. Bowen, A. Bylinkin, J. Castle, S. Khalil, A. Kropivnitskaya, D. Majumder, W. Mcbrayer, M. Murray, C. Rogan, S. Sanders, E. Schmitz, J.D. Tapia Takaki, Q. Wang

Kansas State University, Manhattan, U.S.A.

S. Duric, A. Ivanov, K. Kaadze, D. Kim, Y. Maravin, D.R. Mendis, T. Mitchell, A. Modak, A. Mohammadi

Lawrence Livermore National Laboratory, Livermore, U.S.A.

F. Rebassoo, D. Wright

University of Maryland, College Park, U.S.A.

A. Baden, O. Baron, A. Belloni, S.C. Eno, Y. Feng, C. Ferraioli, N.J. Hadley, S. Jabeen, G.Y. Jeng, R.G. Kellogg, J. Kunkle, A.C. Mignerey, S. Nabili, F. Ricci-Tam, M. Seidel, Y.H. Shin, A. Skuja, S.C. Tonwar, K. Wong

Massachusetts Institute of Technology, Cambridge, U.S.A.

D. Abercrombie, B. Allen, V. Azzolini, A. Baty, G. Bauer, R. Bi, S. Brandt, W. Busza, I.A. Cali, M. D'Alfonso, Z. Demiragli, G. Gomez Ceballos, M. Goncharov, P. Harris, D. Hsu, M. Hu, Y. Iiyama, G.M. Innocenti, M. Klute, D. Kovalskyi, Y.-J. Lee, P.D. Luckey, B. Maier, A.C. Marini, C. Mcginn, C. Mironov, S. Narayanan, X. Niu, C. Paus, C. Roland, G. Roland, Z. Shi, G.S.F. Stephans, K. Sumorok, K. Tatar, D. Velicanu, J. Wang, T.W. Wang, B. Wyslouch

University of Minnesota, Minneapolis, U.S.A.

A.C. Benvenuti[†], R.M. Chatterjee, A. Evans, P. Hansen, J. Hiltbrand, Sh. Jain, S. Kalafut, M. Krohn, Y. Kubota, Z. Lesko, J. Mans, N. Ruckstuhl, R. Rusack, M.A. Wadud

University of Mississippi, Oxford, U.S.A.

J.G. Acosta, S. Oliveros

University of Nebraska-Lincoln, Lincoln, U.S.A.

E. Avdeeva, K. Bloom, D.R. Claes, C. Fangmeier, F. Golf, R. Gonzalez Suarez, R. Kamalieddin, I. Kravchenko, J. Monroy, J.E. Siado, G.R. Snow, B. Stieger

State University of New York at Buffalo, Buffalo, U.S.A.

A. Godshalk, C. Harrington, I. Iashvili, A. Kharchilava, C. Mclean, D. Nguyen, A. Parker, S. Rappoccio, B. Roozbahani

Northeastern University, Boston, U.S.A.

G. Alverson, E. Barberis, C. Freer, Y. Haddad, A. Hortiangtham, D.M. Morse, T. Orimoto, T. Wamorkar, B. Wang, A. Wisecarver, D. Wood

Northwestern University, Evanston, U.S.A.

S. Bhattacharya, J. Bueghly, O. Charaf, T. Gunter, K.A. Hahn, N. Odell, M.H. Schmitt, K. Sung, M. Trovato, M. Velasco

University of Notre Dame, Notre Dame, U.S.A.

R. Bucci, N. Dev, M. Hildreth, K. Hurtado Anampa, C. Jessop, D.J. Karmgard, K. Lannon, W. Li, N. Loukas, N. Marinelli, F. Meng, C. Mueller, Y. Musienko[37], M. Planer, A. Reinsvold, R. Ruchti, P. Siddireddy, G. Smith, S. Taroni, M. Wayne, A. Wightman, M. Wolf, A. Woodard

The Ohio State University, Columbus, U.S.A.

J. Alimena, L. Antonelli, B. Bylsma, L.S. Durkin, S. Flowers, B. Francis, C. Hill, W. Ji, T.Y. Ling, W. Luo, B.L. Winer

Princeton University, Princeton, U.S.A.

S. Cooperstein, P. Elmer, J. Hardenbrook, N. Haubrich, S. Higginbotham, A. Kalogeropoulos, S. Kwan, D. Lange, M.T. Lucchini, J. Luo, D. Marlow, K. Mei, I. Ojalvo, J. Olsen, C. Palmer, P. Piroué, J. Salfeld-Nebgen, D. Stickland, C. Tully

University of Puerto Rico, Mayaguez, U.S.A.

S. Malik, S. Norberg

Purdue University, West Lafayette, U.S.A.

A. Barker, V.E. Barnes, S. Das, L. Gutay, M. Jones, A.W. Jung, A. Khatiwada, B. Mahakud, D.H. Miller, N. Neumeister, C.C. Peng, S. Piperov, H. Qiu, J.F. Schulte, J. Sun, F. Wang, R. Xiao, W. Xie

Purdue University Northwest, Hammond, U.S.A.

T. Cheng, J. Dolen, N. Parashar

Rice University, Houston, U.S.A.

Z. Chen, K.M. Ecklund, S. Freed, F.J.M. Geurts, M. Kilpatrick, W. Li, B.P. Padley, R. Redjimi, J. Roberts, J. Rorie, W. Shi, Z. Tu, A. Zhang

University of Rochester, Rochester, U.S.A.

A. Bodek, P. de Barbaro, R. Demina, Y.t. Duh, J.L. Dulemba, C. Fallon, T. Ferbel, M. Galanti, A. Garcia-Bellido, J. Han, O. Hindrichs, A. Khukhunaishvili, E. Ranken, P. Tan, R. Taus

Rutgers, The State University of New Jersey, Piscataway, U.S.A.

J.P. Chou, Y. Gershtein, E. Halkiadakis, A. Hart, M. Heindl, E. Hughes, S. Kaplan, R. Kunnawalkam Elayavalli, S. Kyriacou, I. Laflotte, A. Lath, R. Montalvo, K. Nash, M. Osherson, H. Saka, S. Salur, S. Schnetzer, D. Sheffield, S. Somalwar, R. Stone, S. Thomas, P. Thomassen, M. Walker

University of Tennessee, Knoxville, U.S.A.

A.G. Delannoy, J. Heideman, G. Riley, S. Spanier

Texas A&M University, College Station, U.S.A.

O. Bouhali[75], A. Celik, M. Dalchenko, M. De Mattia, A. Delgado, S. Dildick, R. Eusebi, J. Gilmore, T. Huang, T. Kamon[76], S. Luo, D. Marley, R. Mueller, D. Overton, L. Perniè, D. Rathjens, A. Safonov

Texas Tech University, Lubbock, U.S.A.

N. Akchurin, J. Damgov, F. De Guio, P.R. Dudero, S. Kunori, K. Lamichhane, S.W. Lee, T. Mengke, S. Muthumuni, T. Peltola, S. Undleeb, I. Volobouev, Z. Wang

Vanderbilt University, Nashville, U.S.A.

S. Greene, A. Gurrola, R. Janjam, W. Johns, C. Maguire, A. Melo, H. Ni, K. Padeken, F. Romeo, J.D. Ruiz Alvarez, P. Sheldon, S. Tuo, J. Velkovska, M. Verweij, Q. Xu

University of Virginia, Charlottesville, U.S.A.

M.W. Arenton, P. Barria, B. Cox, R. Hirosky, M. Joyce, A. Ledovskoy, H. Li, C. Neu, T. Sinthuprasith, Y. Wang, E. Wolfe, F. Xia

Wayne State University, Detroit, U.S.A.

R. Harr, P.E. Karchin, N. Poudyal, J. Sturdy, P. Thapa, S. Zaleski

University of Wisconsin - Madison, Madison, WI, U.S.A.

J. Buchanan, C. Caillol, D. Carlsmith, S. Dasu, I. De Bruyn, L. Dodd, B. Gomber, M. Grothe, M. Herndon, A. Hervé, U. Hussain, P. Klabbers, A. Lanaro, K. Long, R. Loveless, T. Ruggles, A. Savin, V. Sharma, N. Smith, W.H. Smith, N. Woods

†: Deceased
1: Also at Vienna University of Technology, Vienna, Austria
2: Also at IRFU, CEA, Université Paris-Saclay, Gif-sur-Yvette, France
3: Also at Universidade Estadual de Campinas, Campinas, Brazil
4: Also at Federal University of Rio Grande do Sul, Porto Alegre, Brazil
5: Also at Université Libre de Bruxelles, Bruxelles, Belgium
6: Also at University of Chinese Academy of Sciences, Beijing, China
7: Also at Institute for Theoretical and Experimental Physics, Moscow, Russia
8: Also at Joint Institute for Nuclear Research, Dubna, Russia
9: Also at Fayoum University, El-Fayoum, Egypt
10: Now at British University in Egypt, Cairo, Egypt
11: Now at Helwan University, Cairo, Egypt
12: Now at Ain Shams University, Cairo, Egypt
13: Also at Department of Physics, King Abdulaziz University, Jeddah, Saudi Arabia
14: Also at Université de Haute Alsace, Mulhouse, France
15: Also at Skobeltsyn Institute of Nuclear Physics, Lomonosov Moscow State University, Moscow, Russia
16: Also at Tbilisi State University, Tbilisi, Georgia
17: Also at CERN, European Organization for Nuclear Research, Geneva, Switzerland
18: Also at RWTH Aachen University, III. Physikalisches Institut A, Aachen, Germany
19: Also at University of Hamburg, Hamburg, Germany
20: Also at Brandenburg University of Technology, Cottbus, Germany
21: Also at Institute of Physics, University of Debrecen, Debrecen, Hungary
22: Also at Institute of Nuclear Research ATOMKI, Debrecen, Hungary
23: Also at MTA-ELTE Lendület CMS Particle and Nuclear Physics Group, Eötvös Loránd University, Budapest, Hungary
24: Also at Indian Institute of Technology Bhubaneswar, Bhubaneswar, India
25: Also at Institute of Physics, Bhubaneswar, India
26: Also at Shoolini University, Solan, India
27: Also at University of Visva-Bharati, Santiniketan, India
28: Also at Isfahan University of Technology, Isfahan, Iran
29: Also at Plasma Physics Research Center, Science and Research Branch, Islamic Azad University, Tehran, Iran
30: Also at Università degli Studi di Siena, Siena, Italy
31: Also at Scuola Normale e Sezione dell'INFN, Pisa, Italy
32: Also at Kyung Hee University, Department of Physics, Seoul, Korea
33: Also at International Islamic University of Malaysia, Kuala Lumpur, Malaysia
34: Also at Malaysian Nuclear Agency, MOSTI, Kajang, Malaysia
35: Also at Consejo Nacional de Ciencia y Tecnología, Mexico City, Mexico
36: Also at Warsaw University of Technology, Institute of Electronic Systems, Warsaw, Poland
37: Also at Institute for Nuclear Research, Moscow, Russia